

**Master's thesis**

**NTNU**  
Norwegian University of Science and Technology  
Faculty of Engineering  
Department of Energy and Process Engineering

Roshan Jeyakaran

# Fluid structure interaction in circular blade cascade

Master's thesis in Mechanical Engineering

Supervisor: Chirag Trivedi

June 2022



Roshan Jeyakaran

# **Fluid structure interaction in circular blade cascade**

Master's thesis in Mechanical Engineering  
Supervisor: Chirag Trivedi  
June 2022

Norwegian University of Science and Technology  
Faculty of Engineering  
Department of Energy and Process Engineering



Roshan Jeyakaran

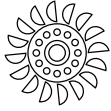
# Fluid structure interaction in circular blade cascade

Master of Science

Department of Energy and Process Engineering  
Faculty of Engineering  
Norwegian University of Science and Technology

Trondheim, June 2022

copyright © 2022 Roshan Jeyakaran



---

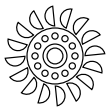
## Abstract

When fluid flows across a structure, unwanted vortices can develop. In the hydropower industry, this is a major problem that can be generated in guide vanes that transverse into the runner, causing vibrations. Though there are several different vortices that can be found in a hydropower plant, this present work investigates von Kármán vortex shedding. Growing energy demand requires a wider operation range of the hydropower plants resulting in higher dynamic loads. Turbine blades are manufactured thinner to reduce costs. As a result, catastrophic structural failures have been reported.

The purpose of this present work is to investigate the fluid structure interaction, to develop a better understanding on the vortex induced vibrations and structural failures. A three-dimensional circular cascade of eight blades is prepared and simulated for a range of velocities to investigate the fluid flow and vortex shedding. Monitored pressure values exhibited oscillation, which indicated vortex shedding. However, further analysis indicated that this was not the case. Modal analysis has been carried out to evaluate the natural frequencies of the eigenmodes, with also an acoustic analysis to account for hydrodynamic damping, by representing the surrounding fluid with an acoustic domain. A harmonic response has been investigated using Macro-Fiber Composite piezoelectric patches to excite the blades at desired frequencies. This was to investigate the frequencies at which frequency lock-in may be expected to occur and thus an indication of which frequency range to avoid. The first bending mode with air and the fifth bending mode in water, both at the trailing edge yielded the greatest amplitude. Moreover, a one-way Fluid-Structure Interaction (FSI) has been carried out to investigate hydrodynamic effects. The blade was prescribed with a motion of the first mode shape, and damping ratio was numerically determined. This analysis indicated negligible damping due to very low amplitudes in the deformation, and

no vortex shedding was observed. A two-way FSI analysis has been carried out to investigate how the fluid flow and vortex shedding interacts with the structure. The model successfully simulated the flow field for a relatively high time step, yielding similar results to one-way FSI and the transient CFD simulations. However, it quickly became unstable for when the time step was reduced. Also, structural analysis showed high stress regions near hub and shroud close to the trailing edge.





---

## Sammendrag

Når væske strømmer over en struktur, kan det utvikles uønskede virvler. I vannkraftindustrien er dette et stort problem som kan genereres i ledeskovler, der virvler går på tvers inn i løperen og forårsaker vibrasjoner. Selv om det er flere forskjellige virvler som kan bli observert, undersøker dette nåværende arbeidet von Kármán virvelavgivelse. Økende energibehov krever et bredere driftsområde for vannkraftverkene, noe som resulterer i høyere dynamiske belastninger. I tillegg produseres turbinblader tynnere for å redusere kostnadene. Som et resultat har katastrofale strukturelle feil blitt rapportert.

Hensikten med dette nåværende arbeidet er å undersøke fluid-struktur interaksjonen, for å utvikle en bedre forståelse av virvelinduserte vibrasjoner og strukturelle feil. En tredimensjonal sirkulær kaskade med åtte blader er forberedt og simulert for en rekke hastigheter for å undersøke strømmingen og virvelavgivelsen. Overvåkede trykkverdier viste oscillasjoner, noe som indikerte virvelavgivelse. Videre analyse tydet imidlertid på at dette ikke var tilfelle.

Modal analyse har blitt utført for å evaluere de naturlige frekvensene til modusformer, med også en akustisk analyse for å ta hensyn til hydrodynamisk demping, ved å representere det omgivende fluidet med et akustisk domene. En harmonisk respons har blitt undersøkt ved å bruke Macro-Fiber Composite (MFC) piezoelektriske patcher for å eksitere bladene ved ønskede frekvenser. Dette var for å undersøke hvilke frekvenser det kan forventes at frekvensinnlåsing vil skje og dermed en indikasjon på hvilket frekvensområde som bør unngås. Den første bøyemodusen med luft og den femte bøyemodusen i vann, begge ved bakkanten, ga størst amplitude. I tillegg er det utført en enveis fluid-struktur interaksjon (FSI) for å undersøke hydrodynamiske effekter. Bladet ble foreskrevet med en bevegelse av den første modusformen, og dempingsforholdet ble numerisk bestemt. Denne

analysen indikerte ubetydelig demping på grunn av svært lave amplituder i deformasjonen, og det ble ikke observert virvelavgivelse.

En toveis FSI-analyse er utført for å undersøke hvordan væskestrømmen og virvelavgivelsen samhandler med strukturen. Modellen har simulert strømningsfeltet for et relativt høyt tidstrinn, og ga resultater som ligner på enveis FSI og de forbigående CFD-simuleringene. Det ble imidlertid raskt ustabil for når tidstrinnet ble redusert. Strukturelle analyser viste også områder med høy spenning nær nav og deksel nær bakkanten.

---

## **Acknowledgments**

This thesis has been written at the Waterpower Laboratory, Department of Energy and Process Engineering at the Norwegian University of Science and Technology (NTNU) in Trondheim. I would like to express my gratitude to the lab and my academic supervisor, Chirag Trivedi, for giving me the opportunity to write my master thesis about an exciting topic, and also for providing guidance and support during my master thesis work. Chirag has always gone out of his way to provide help.

I would also like to express my gratitude to the people at the Waterpower Laboratory for making my final year as a student a great one. Lastly, I would like to extend my thanks to my family and friends for showing me support and patience throughout the year.



---

# Contents

<b>Abstract</b>	<b>i</b>
<b>Sammendrag</b>	<b>iii</b>
<b>Acknowledgments</b>	<b>v</b>
<b>Contents</b>	<b>ix</b>
<b>List of tables</b>	<b>xi</b>
<b>List of figures</b>	<b>xiv</b>
<b>Nomenclature</b>	<b>xv</b>
<b>1 Introduction</b>	<b>1</b>
1.1 Objective . . . . .	4
<b>2 Literature review</b>	<b>5</b>
<b>3 Theory</b>	<b>9</b>
3.1 Fluid-structure interaction . . . . .	9
3.2 Vorticity . . . . .	10

3.3	Secondary flow . . . . .	13
3.4	CFD . . . . .	14
3.5	Turbulence modelling . . . . .	14
3.6	Structural mechanics . . . . .	18
3.7	Vibration of systems . . . . .	19
3.8	Modal Analysis . . . . .	19
3.9	Harmonic Analysis . . . . .	20
3.10	Hydrodynamic damping . . . . .	22
3.11	Acoustic analysis . . . . .	23
<b>4</b>	<b>Numerical setup</b>	<b>25</b>
4.1	Fluid model description . . . . .	25
4.2	Boundary conditions and mesh discretization study . . . . .	28
4.3	Structural model . . . . .	32
4.4	Modal analysis and harmonic response . . . . .	34
4.5	Acoustic model . . . . .	34
4.6	Mesh dependency test . . . . .	35
4.7	FSI setup . . . . .	35
4.8	One-way FSI: Hydrodynamic damping . . . . .	38
4.9	Two-way FSI . . . . .	39
<b>5</b>	<b>Results and discussions</b>	<b>41</b>
5.1	Unsteady CFD simulations . . . . .	41
5.2	Modal analysis . . . . .	45
5.3	Harmonic response . . . . .	50
5.4	Two-way FSI . . . . .	52
5.5	One-way FSI . . . . .	55
<b>6</b>	<b>Conclusions</b>	<b>59</b>

<b>7</b>	<b>Future work</b>	<b>61</b>
	<b>References</b>	<b>62</b>
<b>A</b>	<b>Appendix A – Master thesis agreement</b>	<b>67</b>
<b>B</b>	<b>Appendix B – MATLAB code for FFT</b>	<b>71</b>
<b>C</b>	<b>Appendix C - Ansys codes</b>	<b>75</b>
	C.1 Ansys code for material properties and mesh type . . . . .	75
	C.2 Voltage load application . . . . .	75





---

## List of tables

4.1	Selected boundary conditions and other parameters for the transient simulation. . . . .	29
4.2	Selected time steps for the different velocities. . . . .	30
4.3	Table of calculated values from mesh independence study using procedure by Celik et al. [1]. . . . .	31
4.4	Table of material properties for the piezoelectric material. . .	33
4.5	Selected boundary conditions and other parameters for the transient one-way FSI . . . . .	38



---

## List of figures

1.1	Clouds reveal vortex shedding pattern as wind hits one of the Juan Fernandez Island [2] . . . . .	2
3.1	Flow chart of a two-way FSI process [3] . . . . .	10
4.1	3D model of the test rig. . . . .	26
4.2	Numerical model of blade cascade. . . . .	26
4.3	Overview of CFD mesh. . . . .	26
4.4	Close-up image of blade passage. . . . .	27
4.5	Mesh zoomed in at trailing edge. . . . .	28
4.6	Numerical setup in CFX. . . . .	29
4.7	Mesh model used in FEM solver. . . . .	32
4.8	Zoomed in on piezoelectric patch. . . . .	32
4.9	Mesh dependency test in air . . . . .	36
4.10	Mesh dependency test in water . . . . .	36
5.1	FFT of velocity fluctuations showing . . . . .	42
5.2	Pressure contour showing stagnation points and separation points. . . . .	43

5.3	Isosurface of vortical structures identified by Q-criterion method. No von Kármán vortex street is present. . . . .	44
5.4	Mode shapes observed with air. . . . .	45
5.5	Mode shapes observed with air. . . . .	46
5.6	5 Mode shapes observed with water . . . . .	48
5.7	Total deformation at 1860 Hz and $-179.6^\circ$ , with no surrounding water. . . . .	50
5.8	Total deformation at 2900 Hz and $0.6^\circ$ , with surrounding water. 51	
5.9	Monitored pressure 15 mm downstream of TE. Oscillations onset for smallest timestep. . . . .	53
5.10	Pressure contour at time = 0.18035s. $\Delta t = 10^{-3}$ s. . . . .	54
5.11	Pressure contour at time = 0.1852s. $\Delta t = 5 \cdot 10^{-5}$ s. . . . .	54
5.12	Maximum stress observed near trailing edge. . . . .	54
5.13	FFT applied on velocity fluctuations measured 15 mm downstream of trailing edge . . . . .	55
5.14	Q-criterion used to identify vortical structures downstream of trailing edge. . . . .	56
5.15	Velocity profiles 15 mm downstream of TE . . . . .	57

---

## Nomenclature

### Abbreviation

CAD	Computer aided design
CFD	Computational fluid dynamic
DOF	Degree of freedom
DNS	Direct numerical simulation
FEM	Finite element method
FRR	Frequency Reduction Ratio
FSI	Fluid structure interaction
FFT	Fast fourier transform
GCI	Grid convergence index
LE	Leading edge
LES	Large eddy simulation
M	Modal mass
MFC	Macro fiber composite
NTNU	Norwegian University of Science and Technology
RANS	Reynolds-averaged Navier-Stokes equation
SAS	Scale adaptive simulation

SST	Shear stress transport
T	Time period
t	trailing edge thickness
TE	Trailing edge
U	Freestream velocity
URF	Under relaxation factor

**Latin symbols**

$A$	Area ( $\text{m}^2$ )
$c$	Speed of sound ( $\text{m s}^{-1}$ )
$D$	Diameter (m)
$E$	Young's Moduli (MPa)
$f$	Frequency (Hz)
$G$	Shear moduli (MPa)
$k$	Turbulent kinetic energy ( $\text{m}^2 \text{s}^{-2}$ )
$l$	Length (m)
$p$	Pressure (Pa)
$\bar{p}$	Average pressure (Pa)
$\tilde{p}$	Fluctuating pressure (Pa)
$q_0$	Maximum displacement of blade (mm)
$S$	Symmetric strain rate ( $\text{s}^{-1}$ )
$t$	Time (s)
$w$	Streamwise velocity in z-axis direction ( $\text{ms}^{-1}$ )
$W$	Work

**Dimensionless numbers**

Re	Reynolds number
----	-----------------

St Strouhal number

### **Greek symbols**

$\epsilon$  Rate of dissipation of turbulent kinetic energy ( $\text{m}^2 \text{s}^{-3}$ )

$\phi$  Phase angle ( $^\circ$ )

$\mu$  Dynamic viscosity (Pa s)

$\nu$  Kinematic viscosity (Pa s)

$\nu$  Poisson's ratio (-)

$\Omega$  Antisymmetric strain rate ( $\text{s}^{-1}$ )

$\omega$  Natural frequency (Hz)

$\rho$  Density ( $\text{m}^2 \text{s}^{-1}$ )

$\tau$  Shear stress (Pa)

$\zeta$  Damping ratio (-)

### **Superscripts and subscripts**

1,2,... Indices

$()_{ij}$  Newton suffix

atm Atmospheric

$()'$  Fluctuation of variable

max Maximum

min Minimum

rms Root-mean-square

v Virtual





---

## Chapter 1

---

### **Introduction**

Climate change is one of the greater threats facing the world today. Not only in the form of more extreme weather; it also affects global politics, the economy and quality of life. There is an increased pressure worldwide to reduce fossil energy sources, and transition to more green energy. Intermittent power production from renewable energy sources, such as wind power and solar power, is not stable enough alone to provide electricity for a growing demand for clean energy [4]. Hydropower can produce energy quickly, and water may be stored in reservoirs for when power demand is high. Hydropower is also one of the oldest sources of renewable energy, has been well researched and is considered to be stable. One type of hydraulic turbine, the Francis turbine, has efficiency greater than 90% [5].

However, for hydropower to be in synergy with other power sources and demand, the power outputs of turbines have to be adjusted constantly. This means the turbines have to operate over a wide range, outside of the designed operating point. These fluctuations result in higher dynamic loads. At the same time, it has become common for turbine blades to be made in a more lightweight material and thinner design. This is to reduce material cost and increase hydraulic efficiency, thereby leaving turbine blades to be more susceptible to cyclic stress, resulting in catastrophic failure in blades due to fatigue cracking [6]. This motivates for a better understanding of the fluid flow around the hydraulic turbine blades and the effect fluid flow has on the structure.

The interaction between fluid flow and structure is called Fluid Structure Interaction (FSI). Fatigue and failure of blades may be attributed to this interaction, especially when the structure vibrates close to its natural frequency, causing a resonance phenomenon. During resonance, deformation amplitude and induced loads may be extreme. This is a common problem

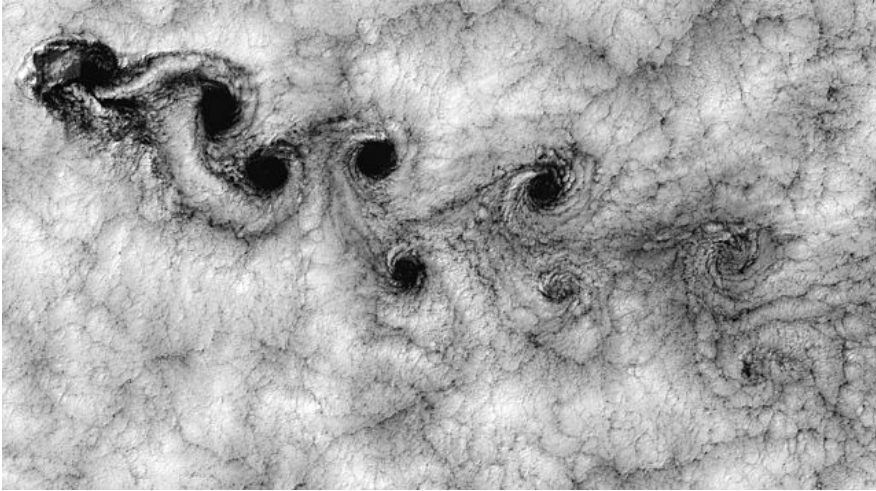


**Figure 1.1:** Clouds reveal vortex shedding pattern as wind hits one of the Juan Fernandez Island [2]

occurring in many fields of engineering, such as bridges. A common example of this phenomenon is the Tacoma Bridge, which collapsed due to oscillations a frequency matching a torsion bending mode.

Vortex induced vibration is a fluid phenomenon, a characteristic flow feature observed in the wake. Figure 1.1 illustrates clouds forming a von Kármán vortex street as wind flows across an island. An article by Griffin et al. [7] attempts to describe the von Kármán vortex shedding phenomena. Shear layers are separated on the upper and lower surface, whilst the velocity gradients in the shear layer cause them to roll into vortex pairs [7]. The article investigated flow over bluff bodies, and suggested that at one point, a vortex will grow in sufficient strength such that it will pull the adjacent vortex across the wake, so that the vortices now have opposite directions in circulation. Due to this, the adjacent vortex will cut free the first vortex. Now, the vortex that has been cut free is shed downstream. This process is repeated and thus an oscillating shedding of vortices occurs. When a vortex is shed, an opposing force acts on the body due to the difference in pressure across the vortex. As the pressure is oscillating, the forces on the blade oscillate, thereby causing vibrations.

The load from flow past the blades is dynamic and may cause the structure to vibrate. Vibrations have two important aspects; the eigenmode and

---

natural frequency. In simpler terms, eigenmodes can be explained as a unique deformation shape characteristic to a vibrating structure. Each eigenmode has its own eigenfrequency, widely known as natural frequency. When a sinusoidal load is applied to the structure, eigenmodes may be excited, resulting in a greater deformation of the structure. Eigenmodes are dependent on characteristics such as surrounding fluid, constraints, material of structure and shape. This means that the natural frequency will depend on the same factors.

When the frequency of the dynamic load is in the proximity of the structure's natural frequency, a resonance phenomenon occurs. Amplitudes may then reach high values and cause structural failure over time. All mechanical systems have some sort of resistance, and so do all materials, such that there is an internal damping. In terms of vibrations, the resistance and internal damping may contribute to preventing catastrophic failure. Damping and resonance is another important parameter for investigating structural vibrations. For fluid flow, the effect of surrounding fluid dominates the damping effects compared to internal damping of materials [8]. This type of damping is called hydrodynamic damping. It is important to understand the shedding frequency of the blades to avoid resonance. This has been investigated by conducting simulations with computational fluid dynamics (CFD) of a circular blade cascade. Turbine blades are in rotation during operation, however this would complicate the simulations. Therefore, the blades are assumed stationary while the water flows past. Hydraulic turbine blades and their trailing edge geometry play a great role in vortex shedding characteristics, such as frequency and amplitude. Therefore, it is important to perform isolated studies to be able to study the parameters of interest.

Investigation of a rotating system would be too demanding, both numerically and experimentally. Bergan et al. [9] suggested a non-rotating axial turbine with an inner and outer tube which would be connected to the blades. Water flow would be in the axial direction, along the tubes. The test rig is a good way to reduce the complexity of the curved geometry of Francis runner blade, which then allows for experimental testing that allows for better understanding and further design improvements. This simplification of the geometry is important as instrumentation should not interfere and disturb the flow field.

## 1.1 Objective

The master thesis is a continuation of the project work carried out during Autumn 2021. As a continuation, the numerical modelling will be of the blade cascade will be done with accurate verification and validation. A literature study will be conducted, amongst other, on fluid-structure interaction in hydro turbines, blade flutter, flow separation, trailing edge vortex, stress and strain, fatigue, resonance, mode-shapes and hydrodynamic damping. Moreover, a numerical model identical to the experimental setup, which is under preparation in the Waterpower Laboratory, will be created. The flow field in the blade cascade will be investigated, using both one-way and two-way fluid-structure interactions. Modal and harmonic analysis will also be performed.

The following sections are partly reused and modified: 2, 3.2, 3.5 3.8 and 3.9. Some parts of chapter 4 will also be in resemblance as similar methodology was implemented.

---

## Chapter 2

---

### Literature review

In this section, previous work on the study of fluid-structure interaction on turbine blades will be summarized. Aspects such as vortex shedding and induced vibration, hydrodynamic damping, structural analysis, modal and harmonic analysis will be of focus. Firstly, literature on vortex shedding is presented, before lock-in and natural frequency is discussed. Literature on hydrodynamic effects in numerical simulations is presented, and finally one-way FSI and two-way FSI is presented.

Sick et al. [10] investigated von Kármán vortex shedding at stay vanes where a validation study was performed on a NACA009 profile, comparing numerical and experimental data. Their main findings was that the vortex structure is resolved well, but not grid independent, when using two million cells. Amplitude of pressure pulsation was found to be highly dependant on the numerical mesh and turbulence model, while the numerically predicted shedding frequency was well predicted and independent on both mesh and turbulence model. Furthermore, boundary layers and vortex shedding region require extremely high grid resolution.

Heskestad and Olberts [11] investigated the effect of trailing edge geometry on vortex induced vibrations on hydraulic turbine blades. The separation points are said to be close to each other, near the vertices of the triangle of the trailing edge. The net effect of this was a reduced vortex strength and excitation force, though an increased shedding frequency was found. For the same trailing edge geometry as the current study, no vortex shedding was observed, due to the separation points being close to each other. Furthermore, they conclude that the vortex strength is a function of distance between separation points, degree of shielding and vortex shedding frequency.

Bergan et al. [9] performed experiments on a submerged, double fixed hy-

drofoil for both a single hydrofoil and a linear cascade with three hydrofoils. A square test section was used for both configurations at the Waterpower Laboratory, NTNU. Two geometries of trailing edge was considered, where the "F1" as described in the paper is a similar geometry as in this present thesis, but the trailing edge thickness is slightly smaller in the present study. Above lock-in velocities, a linear trend was observed for where damping ratio was increasing, which was fairly consistent with earlier investigations. A discontinuity was observed near lock-in region with a sudden jump in both natural frequency and damping ratio for velocities greater than at lock-in region. Additionally, before lock-in velocity, the damping ratio seems to have a small slope but may be considered as close to constant. Furthermore, the difference in scale of hydrofoil investigated in experimental work could affect the damping factor. The linear cascade with three hydrofoils showed similar behaviour, but there was a great level of uncertainty whether this would translate to radial cascade or increased number of blades.

Coutu et al. [12] investigated the hydrodynamic damping of three different hydrofoils with fixed ends, in flowing water. The hydrofoils were excited using Macro Fiber Composites (MFCs) set near the trailing edges to maximize excitation of the first bending mode shape, while keeping the influence of the flow to a minimum. A frequency response function near the first mode of vibration was found, such that the natural frequency and damping ratio could be found. For increasing velocity, Coutu et al. state that it is not clear if the natural frequency varies, because the variations are small enough to stay within the error interval. On the other hand, with increasing velocity, a clear trend of increased damping was observed. At resonance, the amplification factor was significantly reduced with an increase in damping. Furthermore, only one mode shape of the structure was investigated, as it is the shape which results in faster failure.

Liang et al. [13] conducted numerical studies on a Finite Element Method model to investigate the influence of water on a model Francis runner. The paper exhibited good agreement between experimental and numerically estimated eigenfrequencies and the mode shapes, though the numerically estimated values were overpredicted. Moreover, a harmonic response was conducted on the model using dynamic pressure load from an unsteady CFD simulation. The paper states that there is still a gap in how well the information may be translated to a more realistic scale.

Tengs et al. [14] performed a one-way coupled FSI analysis of one blade using the same geometry as in the current study. The blade was given a prescribed frequency and amplitude determined by a modal analysis, and the

---

focus was on investigating hydrodynamic effects at different velocities. Hydrodynamic damping was found to be a function of flow velocity only, though for small deflections. A region of constant damping was found before lock-in region, while damping was found to be linearly increasing after lock-in. The author states an investigation needs to be done where the configuration is in closer resemblance of a Francis turbine, such as with a circular cascade.

Liaghat et al. [15] conducted a two-way FSI analysis in order to investigate vibration and damping of an oscillating hydrofoil for different flow velocities. The main observations are that maximum amplitude of the vibration of hydrofoil and response frequency of hydrofoil, decrease with increasing flow velocity. Only the first mode was investigated. Furthermore, a linear relationship is reported between damping ratio and flow velocity. This is in agreement with Tengs [14] for velocities above lock-in region. Additionally, higher velocities required finer mesh resolution of the fluid.

Several studies on FSI analysis have been conducted on submerged hydrofoils, however there are no studies on a circular blade cascade with eight blades. Despite no vortex shedding being observed in the experimental work by Heskestad and Olberts for the similar trailing edge geometry, it is still important to ensure this in a CFD simulation. This thesis aims to investigate the aforementioned configuration, vortex shedding, hydrodynamic damping, structural and vibrational analysis.





---

## Chapter 3

---

### Theory

*The following section presents relevant theory which serves as a background information required to understand the physics and numerical modelling used, but to also understand and explain results and observations from the simulations. Firstly, an overview of the concept of fluid structure interaction is explained, along with the algorithm of two-way fluid structure interaction. Vortex formation and lock-in theory is then presented, before turbulence modelling in computational fluid dynamics is presented. Furthermore, failure due to fatigue is addressed before numerical structural mechanics theory is presented. Governing equations are then presented, for structural, modal and harmonic response analysis. Moreover, a section on hydrodynamic damping is presented where the added mass effect and damping ratio is explained, before an explanation of how this damping may be addressed in the numerical simulations.*

#### 3.1 Fluid-structure interaction

Fluid-Structure Interaction (FSI) is a broad term denoting the interaction between fluids and the structures. It is a good way to understand how the two components act on each other Benra et al. [3]. There are 3 ways to couple the fluid and structural systems. One way coupling consists of a CFD code and FEM code, to solve one domain first. Information is passed from this domain to the second domain and solved. This involves no feedback between domains. An example is pressure load from CFD simulation imported as a load in a FEM simulation. One-way coupling is the most prevalent way of FSI-analysis. Two-way FSI transfers information between the fluid and structural domain, hence the name, and there is also coupling iterations for the transfer of information. System Coupling is a tool inside ANSYS used to

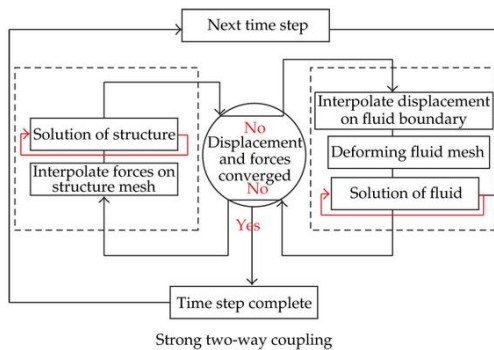


**Figure 3.1:** Flow chart of a two-way FSI process [3]

couple the domains. Fully coupled system is used for non-viscous flow. This is not relevant to this paper and the reader is recommended to read Benra et al. for a more in-depth explanation of coupling in a FSI-analysis.

The process for a two-way coupled FSI is shown in 3.1. Within one time step, a converged fluid flow field is required to generate forces acting on the structure. These forces are then interpolated onto the mesh of the structural domain. A converged solution with the applied load is then required to output structural displacement. This displacement is then interpolated on the fluid mesh. As the fluid and structural domains are strongly coupled in blade deformation, stagger iterations are used to iterate the interpolation such that the changes in the force and displacement are below the set criteria. The next time step may then be launched. This is an iterative implicit process as the coupling iterations are used rather than for explicit where only one iteration is used to solve the information transfer between the two domains. These cases of implicit and explicit methods is not the same as for the solver used but rather the formulation of the discretization of transient terms.

## 3.2 Vorticity

Vorticity is the curl of velocity, and is associated with a rotating motion of fluid. The vorticity vector is defined as

$$\zeta = \nabla \times \mathbf{u} \quad (3.1)$$

and rate of rotation vector is defined as

$$\boldsymbol{\omega} = \frac{1}{2}\boldsymbol{\zeta} \quad (3.2)$$

The vector describes the rotating motion of a fluid particle. Regions with zero vorticity is called irrotational flow, whilst regions with nonzero vorticity is called rotational flow. For a uniform flow over a blunt body, the flow far away is irrotational while the flow inside the boundary layer is considered rotational flow. The components of the vorticity vector is a sum of rate of rotation of two perpendicular fluid lines [16]. To understand the dynamics of vorticity, one can derive the equation for rate of change of vorticity by applying curl-operation on the Navier-Stokes equation. For incompressible, viscous flow with no body forces, the equation is as follows

$$\frac{\partial \boldsymbol{\omega}}{\partial t} + (\mathbf{u} \cdot \nabla)\boldsymbol{\omega} = (\boldsymbol{\omega} \cdot \nabla)\mathbf{u} + \mu \nabla^2 \boldsymbol{\omega} \quad (3.3)$$

where the terms are:

- $\frac{\partial \boldsymbol{\omega}}{\partial t}$  is the change in rate due to transient vorticity field.
- $(\mathbf{u} \cdot \nabla)\boldsymbol{\omega}$  describes the rate of change due to convection.
- $(\boldsymbol{\omega} \cdot \nabla)\mathbf{u}$  describes stretching and tilting of fluid particle due to velocity gradients.
- $\mu \nabla^2 \boldsymbol{\omega}$  is viscous diffusion of vorticity.

Considering flow in two-dimensional along a flat plate, the velocity profile of the boundary layer has one vorticity component perpendicular to the two-dimensional x-y axis.

$$\zeta = \frac{\partial v}{\partial x} - \frac{\partial u}{\partial y} \approx -\frac{\partial u}{\partial y} \quad (3.4)$$

When this is substituted into shear stress relation for Newtonian fluid, it gives:

$$\tau_{x,y} = \mu \frac{\partial u}{\partial y} = -\mu \omega_z \quad (3.5)$$

The boundary layer equation may be expressed as,

$$u \frac{\partial u}{\partial x} + v \frac{\partial u}{\partial y} = \frac{-1}{\rho} \frac{\partial p}{\partial x} + \nu \frac{\partial}{\partial y} \left( \frac{\partial u}{\partial y} \right) \quad (3.6)$$

Considering the boundary layer equation at  $y = 0$ , applying the no-slip condition, such that velocity is zero, and substituting in equation 3.5. This gives,

$$\frac{1}{\rho} \frac{\partial p}{\partial x} = \mu \frac{\partial^2 u}{\partial y^2} \Big|_{y=0} = -\mu \frac{\partial \omega_z}{\partial y} \Big|_{y=0} \quad (3.7)$$

It can be seen from equation 3.7 that vorticity develops from applying the no-slip condition at the wall, and it is diffused normal to the wall due to adverse pressure gradient in streamwise direction. This means for greater adverse pressure gradient, the fluid particle rotates clockwise at a greater rate.

Flow separation occurs due to adverse pressure gradients in the boundary layer. When  $\tau_{wall} = 0$ , flow separation occurs. Shear layers develop at the separation points that roll up and form vortices in the wake [16]. These alternate in forming at separation points at upper and lower side of objects, at a frequency called shedding frequency. The pattern formed by the alternating shedding in the wake is called a von Kármán street. When a vortex is shed, a reaction force is exerted on the object in the transverse direction. The direction is alternated accordingly to where the vortex is shed. This alternating force causes the object to vibrate. The vortex shedding frequency,  $f_s$  is determined by

$$f_s = St \frac{U}{L} \quad (3.8)$$

where  $St$  is the non-dimensional Strouhal number,  $U$  is freestream velocity and  $L$  is characteristic length of object. Vortex shedding can be found in many areas of hydraulic machinery, such as at the trailing edges of runner blades, guide vanes and stay vanes.

Specifically for Francis turbine blades, Brekke [17] provided an empirical formula for determining shedding frequency for different trailing edge geometries. It is given by,

$$f_s = 190 \frac{B}{100} \frac{U}{t + \delta_v} \quad (3.9)$$

where  $B$  is a constant determined by geometry of trailing edge.  $U$  is the freestream velocity,  $\frac{190}{100}$  is the Strouhal number,  $t$  is thickness of trailing edge and  $\delta_v$  is the virtual boundary layer thickness. Virtual boundary layer thickness is given by the equation,

$$\delta_v = 0.643 \frac{1}{8} \frac{0.37c}{Re^{\frac{1}{5}}} \quad (3.10)$$

The empirical formula for shedding frequency is derived from research on simplified hydrofoils, where upstream of trailing edge is rectangular in shape. Blades in hydraulic machinery are more complex than this, in addition to only being two-dimensional. Therefore, these empirical formulas should be with caution and compare values to numerical or experimental data.

Lock-in is a phenomena that occur when shedding frequency in the flow matches the natural frequency of the structure, notably over a range of operating velocities. For this region, the Strouhal equation is no more valid. If the shedding frequency matches the eigenfrequency, and the structure is not excited on the node, resonance phenomena may occur. This may result in high vibration amplitudes causing cracks and eventually bring the structure to failure [14]. Pre-mature failure has been reported for turbines in which lock-in occur. Due to the presence of lock-in, the behaviour of hydrodynamic damping is affected. The damping ratio is near to constant under lock-in velocity but is linearly increasing for greater velocities. Therefore it is important to study hydrodynamic damping with respect to the lock-in region and velocity.

Lock-in velocity may be estimated by using Brekke's empirical equation for when shedding frequency is equal to eigenfrequency:

$$v_{li} = f_s \frac{100(t + \delta_v)}{190B}, \quad (3.11)$$

where  $v_{li}$  is the lock-in velocity,  $f_s = f_n$ .

### 3.3 Secondary flow

In addition to von Kármán vortex shedding, there is a wide range of other secondary flow structures that may be observed in a turbine passage. These vortex structures have been studied and researched since it is a source of pressure loss. According to Butler and Sharma [18], secondary flow losses account for 30-50% of total pressure loss, which justifies the importance of the research on this.

Although there has been presented several different models of secondary flows throughout the years, the most fundamental flow phenomenon such as horseshoe vortex and passage vortex have an established model and will be presented.

These vortex structures appear in highly loaded turbine cascade with a low aspect ratio. For hydraulic axial turbines, these secondary flow struc-

tures may not appear as clearly in the passage since hydraulic turbines operate with a high aspect ratio and large chord length. However, the physics behind the vortex development and interactions is the same and will be presented as similar vortex structures may be observed in the present work.

The horseshoe vortex is a well known phenomena in fluid dynamics. This phenomena occur in the boundary layer flow around an obstacle [19]. This case, the obstacle is the blade. As the flow approaches the leading edge, the three-dimensional boundary layer separate due to an adverse pressure gradient. The flow is convected around the blade, rolling and wrapping itself around the blade such that the structure resembles a horseshoe.

### 3.4 CFD

Computational fluid dynamics is a powerful tool which utilizes numerical simulation to analyze systems that involve fluid flow and heat transfer, and the associated phenomenon such as chemical reactions. ANSYS CFX uses the finite volume method, a formulation of finite difference [20]. This is used to discretize the governing equations of fluid flow. A numerical grid, namely a mesh, represents the fluid domain, where each cell expresses conservation properties of equations. The accuracy in numerically solving the equations is mainly due to number of elements. A fine mesh, containing a large amount of elements, would capture large gradients better than a mesh containing less elements. However, too many elements results in increased computational time, and therefore the optimal mesh is fine in areas of large gradients while areas of smaller changes have coarser mesh.

### 3.5 Turbulence modelling

Turbulence is a complex subject and is not fully understood, but has some characteristics that is understood. It is an irregular flow with fluctuating velocity and pressure, in both space and time. Hence, it is often characterized as chaotic. It is a transient, three-dimensional phenomenon at high Reynolds numbers [21]. In contrast to turbulent flow, there is laminar flow with a low Reynolds number. Reynolds number is a non-dimensional quantity expressed as:

$$Re = \frac{\rho U L}{\mu} \quad (3.12)$$

where the equation is a ratio between inertial and viscous forces.  $U$  is characteristic velocity,  $L$  is the characteristic length scale of the mean flow and  $\nu$  is the kinematic viscosity. The reader is referred to [21] for an introduction into turbulent flows.

Reynolds decomposition is a technique applied to separate the fluctuating and mean parameters of a turbulent flow. These flow variables can be velocity components, pressure, temperature and density. In a statistically steady flow, every variable may be written as a sum of two terms: a time-averaged term and a fluctuating term, which fluctuates around the time-averaged [21]. This may be exemplified as,

$$\phi(x_i, t) = \Phi(x_i) + \phi'(x_i, t) \quad (3.13)$$

where  $\Phi$  is the mean or time-averaged part of  $\phi$ , and  $\phi'$  is the fluctuation.  $\Phi$  is averaged as

$$\Phi(x_i, t) = \lim_{T \rightarrow \infty} \frac{1}{T} \int_0^T \phi(x_i, t) dt \quad (3.14)$$

where  $t$  is time. For unsteady flows, it is not possible to use time-averaging as above, so ensemble averaging may be used instead to express  $\Phi$  as:

$$\Phi(x_i, t) = \lim_{T \rightarrow \infty} \frac{1}{N} \sum_{n=1}^N \phi(x_i, t) \quad (3.15)$$

where  $N$  is the number of ensemble members. This number must be large enough in order to eliminate fluctuating effects. Einstein notation may be used for shorter notation. Applying Reynolds decomposition to the continuity equation and Navier-Stokes equations yields the Reynolds-Average Navier-Stokes equations, denoted as RANS equations. The velocity components and pressure may be expressed as:

$$u = U + u' \quad v = V + v' \quad w = W + w' \quad p = P + p'. \quad (3.16)$$

As mentioned above, time averaging eliminated the fluctuating parts such that the time averaged continuity equation becomes:

$$\nabla(\mathbf{U}) = 0 \quad (3.17)$$

and time-averaged Navier-Stokes equations for the x, y and z components become

$$\begin{aligned} \frac{\partial U}{\partial t} + \nabla(U\mathbf{U}) = & \frac{-1}{\rho} \left( \frac{\partial P}{\partial x} + \nu \nabla^2(U) \right. \\ & \left. + \left[ -\frac{\partial(\overline{u'^2})}{\partial x} - \frac{\partial(\overline{v'u'})}{\partial y} - \frac{\partial(\overline{u'w'})}{\partial z} \right] \right) \end{aligned} \quad (3.18)$$

$$\begin{aligned} \frac{\partial V}{\partial t} + \nabla(V\mathbf{U}) = & \frac{-1}{\rho} \left( \frac{\partial P}{\partial y} + \nu \nabla^2(V) \right. \\ & \left. + \left[ -\frac{\partial(\overline{v'^2})}{\partial x} - \frac{\partial(\overline{v'u'})}{\partial y} - \frac{\partial(\overline{v'w'})}{\partial z} \right] \right) \end{aligned} \quad (3.19)$$

$$\begin{aligned} \frac{\partial W}{\partial t} + \nabla(W\mathbf{U}) = & \frac{-1}{\rho} \left( \frac{\partial P}{\partial z} + \nu \nabla^2(W) \right. \\ & \left. + \left[ -\frac{\partial(\overline{w'^2})}{\partial x} - \frac{\partial(\overline{w'u'})}{\partial y} - \frac{\partial(\overline{w'v'})}{\partial z} \right] \right) \end{aligned} \quad (3.20)$$

This has resulted in new terms, which appear in the squared brackets. They represent the turbulent stresses in the RANS equation, where they also are called Reynolds stresses. They may be written using tensor notation as:

$$\overline{\rho u'_i u'_j} \quad (3.21)$$

These additional stresses result in an unclosed set of momentum equations, as there are more variables than equations. Therefore, turbulence models are used to model these Reynolds stresses in order to close the set of equations.

RANS models are considered to be the norm for general applications due to the computational resources not being as costly [20]. The most validated and tested models are the two-equation models  $k - \epsilon$ ,  $k - \omega$  and  $SSTk - \omega$ . The  $k - \epsilon$  model consists of an equation for turbulent kinetic energy,  $k$ , and dissipation rate of turbulent energy,  $\epsilon$ . The  $k - \omega$  model consists of an equation for  $k$  and turbulence frequency  $\omega = \frac{\epsilon}{k}$ . Menter's shear stress transport (SST)  $k - \omega$  model is a combination of the two previously mentioned two-equation models [22].  $k - \omega$  model is used for near-wall regions as it handles adverse pressure gradients near boundary layers well, whilst  $k - \epsilon$  model is



used for fully turbulent regions far away from the wall. This allows for using the advantages of both of these models. The weakness of the  $k-\omega$  model is in solving fully turbulent free-stream regions and the weakness of  $k-\epsilon$  model is adverse pressure gradients at boundary layers near walls [20]. Furthermore, the Reynolds stresses are computed with the Boussinesq expression:

$$-\overline{\rho u'_i u'_j} = 2\mu_T S_{ij} - \frac{2}{3}\rho k \delta_{ij} = \mu_T \left( \frac{\partial U_i}{\partial x_j} + \frac{\partial U_j}{\partial x_i} \right) - \frac{2}{3}\rho k \delta_{ij} \quad (3.22)$$

$$S_{ij} = \frac{1}{2} \left( \frac{\partial U_i}{\partial x_j} + \frac{\partial U_j}{\partial x_i} \right) \quad (3.23)$$

where  $\mu_T$  is the eddy viscosity,  $\delta_{ij}$  is the Kronecker delta and  $S_{ij}$  is the mean rate of strain. The turbulent kinetic energy is modelled by the equation:

$$\frac{\partial \rho k}{\partial t} + \nabla \cdot (\rho k \mathbf{U}) = \nabla \cdot \left[ \left( \mu + \frac{\mu_T}{\sigma_k} \right) \nabla(k) \right] + P_k - \beta^* \rho k \omega \quad (3.24)$$

$$P_k = 2\mu_T S_{ij} S_{ij} - \frac{2}{3}\rho \frac{\partial U_i}{\partial x_j} \delta_{ij} \quad (3.25)$$

$P_k$  is a term for turbulent kinetic energy production, commonly termed as a production term. The other transport equation comes from the relationship  $\omega = \frac{\epsilon}{k}$ , substituted into the  $\epsilon$  transport equation such that the  $\omega$  transport equation is described as:

$$\begin{aligned} \frac{\partial \rho \omega}{\partial t} + \nabla \cdot (\rho \omega \mathbf{U}) = & \nabla \cdot \left[ \left( \mu + \frac{\mu_T}{\sigma_{\omega,1}} \right) \nabla \omega \right] + \gamma_2 \left( 2\rho S_{ij} S_{ij} \right. \\ & \left. - \frac{2}{3}\rho \frac{\partial U_i}{\partial x_j} \delta_{ij} \right) - \beta_2 \rho \omega^2 + 2 \frac{\rho}{\sigma_{\omega,2} \omega} \frac{\partial k}{\partial x_k} \frac{\partial \omega}{\partial x_k} \end{aligned} \quad (3.26)$$

$\sigma_k, \sigma_{\omega,1}, \sigma_{\omega,2}, \gamma_2, \beta$  and  $\beta^*$  are model constants. Several modifications have been implemented since it was introduced by Menter in 1993 [22], to improve performance. One of the improvements is the implementation of blending function to have a smooth transition between the two models for when solving the respective regions.

### 3.6 Structural mechanics

Structural failure is as mentioned earlier a problem in the hydropower industry, as much as in most other industries. Structural failure can be sorted into two types: failure due to static load and dynamic load. Although static loads exceeding the yield strength of material is a significant problem, it is rare in turbines. On the other hand, dynamic loads are the dominant problem where fatigue is relevant. Fatigue is a consequence of repeated cyclic loads. The magnitude of stress in the cyclic stress is normally low, but it is rather the number of cycles that brings the structure to failure. Plastic deformation is when a load exceeds yield strength. The pressure loads in the fluid flow, which fluctuate, may be integrated such that it corresponds to the cyclic stresses in the material.

If a system is exposed to several number of stress conditions, this accumulated damage may be estimated by Miner-Palmgren rule, given by the eq.

$$\sum_{i=1}^k \frac{n_i}{N_i} = C \quad (3.27)$$

where  $n_i$  is the number of stress cycles at load  $i$  and  $N_i$  is the number of stress cycles to failure at load  $i$ . At  $C = 1$ , the material failure is assumed to occur.

Governing equations that are used in structural mechanics will be presented in the later sections.

Finite element method, or FEM, is used to solve more complex structural analysis problems. It was developed in the 1960s by different scientists, while the first book to be published was in 1967 by Zienkiewicz. As the name may indicate, the method divides the structure into finite elements that is connected at a finite number of nodes. This may be visualized as a network nodes connected by springs. The springs are edges of the elements while the nodes are the masses within the FEM. Loads are applied on the nodes, and material properties determine the stiffness and damping of the springs. The load will put stresses on the springs and deflect according to their stiffness.

Governing equations and boundary conditions may be used to describe the motion. FEM approximates the equation of motion and boundary conditions as a set of algebraic equations that can be solved numerically. For complex structures, a large number of elements should be used to have an accurate result and to discretize the governing equations. This would be

troublesome by hand and would require computers to solve this.

In a structural analysis, stress and strain due to external loads is interesting to investigate. Stress due to flow field is a bigger concern than the strain as it is usually negligibly low. When evaluating the stress tensors, one must evaluate the nine components in that makes up a stress matrix. This would require nine different plots to evaluate. Equivalent stress allows one to look at one value. One equivalent stress is the von Mises stress  $\sigma_v$ . This value may be used to determine material failure. Assume a matrix containing stress components in directions x, y and z:

$$\begin{bmatrix} \sigma_{xx} & \sigma_{xy} & \sigma_{xz} \\ \sigma_{yx} & \sigma_{yy} & \sigma_{yz} \\ \sigma_{zx} & \sigma_{zy} & \sigma_{zz} \end{bmatrix} \quad (3.28)$$

von Mises stress may then be calculated by:

$$\sigma_v = \sqrt{\frac{(\sigma_{xx} - \sigma_{yy})^2 + (\sigma_{yy} - \sigma_{zz})^2 + (\sigma_{zz} - \sigma_{xx})^2 + 6(\sigma_{xy} + \sigma_{yz} + \sigma_{zx})^2}{2}} \quad (3.29)$$

### 3.7 Vibration of systems

Stationary regions of a vibrating structure are called nodes. This is relevant for the resonance phenomena. Resonance occur when the eigenfrequency and load frequency matches, but it is also necessary for the load to be places away from the node to excite the corresponding eigenmode. For disc-like structures such as turbines, this concept may be generalized to Nodal diameters (ND), where the mode shapes contain lines of zero displacement. If  $n$  NDs are present, the motion may be described as in the form of  $a \cos \theta$  where  $a$  is a function of radial and axial coordinates. For  $n = 0$ , the motion is axisymmetric. For  $n > 0$ , there are two independent modes of vibration at each natural frequency that correspond to the cosine and sine mode shapes. For axisymmetric structures, the angular position of the node lines are determined by the location of load excitation.

### 3.8 Modal Analysis

As mentioned earlier, mechanical vibrations involve two main parameters, eigenmodes and natural frequencies. An undamped structure with no

external load may be described by the equation of motion, in matrix notation as [23]:

$$M\ddot{x} + Kx = 0 \quad (3.30)$$

where  $x$  is a vector containing all degrees of freedom.  $M$  is the mass matrix, containing the mass of the structure.  $K$  is the spring-constant acting as dampers. For a linear system, free vibrations are in harmonic form:

$$x = u_j \cos(\omega_j t) \quad (3.31)$$

where  $u_j$  is the eigenvector or eigenmode, representing deformed vibrating shape for  $j^{th}$  natural frequency  $\omega_j$ . Introducing equation 3.31, the equation of motion may be rewritten as

$$(K - \omega_j^2 M)u_j = 0 \quad (3.32)$$

Considering non-trivial solutions to this equation, the eigenvalue problem becomes:

$$|K - \omega_j^2 M| = 0 \quad (3.33)$$

The solution of this equation, for  $n$  DOFs gives  $n$  eigenvalues, values of  $\omega^2$ . This may then be used to solve for eigenvector, or eigenmodes  $u_j$ . Furthermore, natural frequencies can then be calculated using

$$f_j = \frac{\omega_j}{2\pi} \quad (3.34)$$

### 3.9 Harmonic Analysis

Harmonic analysis is used to determine a steady-state response of a linear structure to sinusoidal loads [23]. Revisiting equation of motion, it may be rewritten in a more general form:

$$M\ddot{x} + C\dot{x} + Kx = F \quad (3.35)$$

In this more general equation,  $F$  is a vector containing external forces at every DOF.  $C$  is a damping matrix containing information on the damping effects. An assumption is made that loads and displacements vary sinusoidally at the same frequency but at different phase. A complex notation would be more fitting to use:

$$x = a_x(\cos\phi + i\sin\phi)e^{i\Omega t} \quad (3.36)$$

$$F = a_F(\cos\psi + i\sin\psi)e^{i\Omega t} = (F_1 + iF_2)e^{i\Omega t} \quad (3.37)$$

where amplitude is denoted by  $a$ , while  $\phi$  and  $\psi$  is the phase of the DOFs and loads respectively. The general can now be rewritten as

$$[K - \Omega^2 M + i\Omega C](x_1 + ix_2) = F_1 + iF_2 \quad (3.38)$$

which may be solved to find the DOFs vectors  $(x_1 + ix_2)$ . The solution is steady state and in the frequency domain rather than time-domain.

Piezoelectric Macrofiber Composites (MFCs) have been extensively used, in experiments to provide excitation at specific frequencies. This allows for measurements when damping is large. This experimental method has been previously used by Couthu et al. and more. In order to account for this setup, it has been included in the numerical modelling. The direct piezoelectric effect is when mechanical stresses arise due to an external load exerted on the piezoelectric body induce a corresponding electric voltage. The inverse piezoelectric effect is when an electric voltage is applied to a piezoelectric body resulting in the geometry to deform. If the body is constrained, reaction forces act on the body. The governing equations for elastic and electric properties are, in matrix notation:

$$[D] = [d]T + [\epsilon]^T E \quad (3.39)$$

$$[S] = [s]^E T + dE \quad (3.40)$$

$D$  is the electric flux density, or also known as dielectric displacement.  $T$  is mechanical stress,  $E$  is the electric field,  $S$  is strain,  $d$  is the piezoelectric charge coefficient,  $\epsilon^T$  is dielectric permittivity (constant T) and  $s^E$  is the elastic coefficient for a constant E.

Previous experiments at the Waterpower Laboratory have used patches from the P-876 series from PI, which is made of the piezoelectric material PIC-255. These exhibit a  $d_{31}$  effect such that the deformation occur perpendicular to the electric field. The material properties of the piezoelectric PIC-255 are given later in chapter 4.3, where properties are from the producer except for the Poisson ratio which was found in Krommer et al. [24].

### 3.10 Hydrodynamic damping

Hydrodynamic damping is the viscous damping due to presence of water surrounding the structure, contributing to reducing the frequency at which the blade vibrate at [8]. Adding to the concept of spring-mass system from chapter 3.5, the damping may be considered as an added mass effect. In air, the natural frequency is given by

$$f_{n,air} = \sqrt{\frac{k}{m}} \quad (3.41)$$

where the important relation is the relationship of natural frequency being proportional to square root of the reciprocal of mass. As the mass of surrounding fluid is considered as added mass  $m'$  that is being accelerated with the body. Natural frequency for submerged structure may be written as

$$f_{n,water} = \sqrt{\frac{k}{m + m'}} \quad (3.42)$$

This is the added mass effect, and as the denominator, total mass, has increased, natural frequency is reduced with the presence of surrounding water [23]. This reduction may be expressed through a ratio called Frequency Reduction Ratio (FRR), which compares it to with no surrounding water.

$$FRR = 1 - \frac{f_{n,water}}{f_{n,air}} \quad (3.43)$$

Recall that a second order oscillating system may be described as the following:

$$M\ddot{x} + C\dot{x} + Kx = F \quad (3.44)$$

The dot notation represents the time derivative. The structural deflection is assumed to follow a periodic with amplitude  $x_0$  and frequency  $\omega$ . The damping ratio for the second order system is defined as

$$\zeta = C(2M\omega)^{-1} \quad (3.45)$$

Assuming linear behaviour, the structural deflection may be decomposed into a sum of different modes which vibrates at its natural frequency. As  $W = \int Fdx$ , one can impose superposition and integrate the left-hand side of the second order equation. Only the first order term will give a non-zero value. For a vibration period, this gives  $W = C\pi\omega q_0^2$ . Additionally, the hydrodynamic work onto the fluid may be defined as:

$$W = - \int_0^T \int_A p \cdot \dot{x}_n dA dt \quad (3.46)$$

where the force has been rewritten as  $\int p dA$ ,  $T$  is one period,  $p$  is fluid pressure and  $\dot{x}_n$ . Combining these variations of hydrodynamic work gives the hydrodynamic damping ratio definition;

$$\zeta = \frac{W}{2\pi M \omega^2 q_0^2} \quad (3.47)$$

Where the denominator is used to normalize the work,  $\omega$  is the natural frequency and  $q_0$  is the maximum displacement of the blade.

Hydrodynamic fluttering is an phenomena which denotes an unstable vibration of a system and a negative damping effect. This means, for certain cases of requirements, the fluid flow would transfer energy to the hydrofoil blade, rather than absorbing energy as is the case for hydrodynamic damping. By assuming an harmonic motion for the blade, blade velocity and similarly for the force though with a phase angle  $\Delta\phi$  such that  $F = F_0 \sin(\omega t + \Delta\phi)$ . Combining this with the equation for work, and solving the integral work one period gives that work may be rewritten as:

$$W = \omega x_0 F_0 \sin(\Delta\phi) \quad (3.48)$$

From this equation, it can be observed that the phase difference  $\Delta\phi$  is the controlling variable. This means a negative phase difference indicates the surrounding water is absorbing energy and thus damping the vibration. A positive phase difference would indicate the structure to absorb energy - this would be the case of fluttering. Despite this, all simulations are assumed to expect damping.

### 3.11 Acoustic analysis

Acoustic analysis is about understanding how information propagates through a medium, such as water [14]. This may be modeled by use of the Helmholtz equation,

$$\nabla^2 p' - \frac{1}{c^2} \frac{d^2 p'}{dt^2} + \nabla \cdot \left[ \frac{4\mu}{3} \nabla(\nabla \cdot v') \right] = 0 \quad (3.49)$$

where  $p'$  and  $v'$  are pressure and velocity fluctuations respectively,  $c$  is the speed of sound in the medium,  $\mu$  is dynamic viscosity of medium. This equation can be written in matrix form, and coupled with the second-order general equation of motion:

$$\left( -\omega^2 \begin{bmatrix} M_s & 0 \\ M_{fs} & M_a \end{bmatrix} + i\omega \begin{bmatrix} C_s & 0 \\ 0 & C_a \end{bmatrix} \begin{bmatrix} K_s & K_{fs} \\ 0 & K_a \end{bmatrix} \right) \begin{bmatrix} u \\ p \end{bmatrix} = \begin{bmatrix} F_s \\ F_a \end{bmatrix} \quad (3.50)$$

This equation solves for acoustic pressure propagation in the acoustic domain, and structural deformation and most importantly, also the interaction between the acoustic and structural domain such as the added mass effect.



## Numerical setup

*Numerical setup describes the modelling approach taken for the simulations. Firstly, the fluid model is considered, describing the geometry and mesh used. The  $y^+$  values is evaluated, before prescribed boundary conditions and numerical schemes are presented. There is a focus on the time step such that vortex shedding is captured. A mesh discretization study with the calculated parameters are shown. The chapter then describes the numerical model used in the FEM solver, along with mesh used for the various cases. A short explanation on piezoelectric patches is given. The numerical setup, including solvers and constrains, used is presented before the acoustic model is described. A mesh sensitivity study is presented for the FEM model. Furthermore, the FSI setup is described for both 1-way and 2-way FSI, along with description of how this is conducted within CFX. Preliminary simulations are also discussed as some input parameters are case sensitive and must be adjusted.*

### 4.1 Fluid model description

The numerical simulations are based on the blade geometry designed for Francis-99 project. It is a symmetric hydrofoil without camber. The thickness of TE is kept at 3.8 mm, 270 mm chord length. The leading edge is defined by an ellipse of 12 mm minor axis and 32 mm major axis. The span length is 115 mm. Moreover, 10% the trailing edge is cut off such that there are no two sides forming a sharp edge, causing singularities. This is a simplification that has been done to simplify the meshing procedure.

Moreover, there is a radius of around 20 mm near the trailing edge before the two surfaces meet. Upper and lower surface of the trailing edge forms a

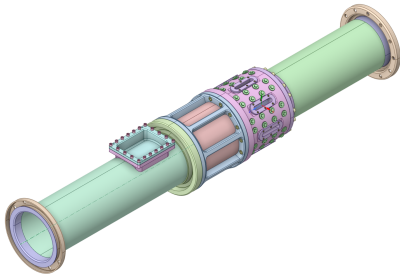


**Figure 4.1:** 3D model of the test rig.

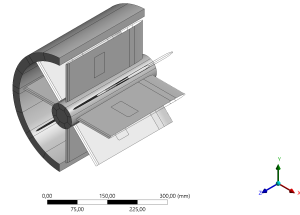


**Figure 4.2:** Numerical model of blade cascade.

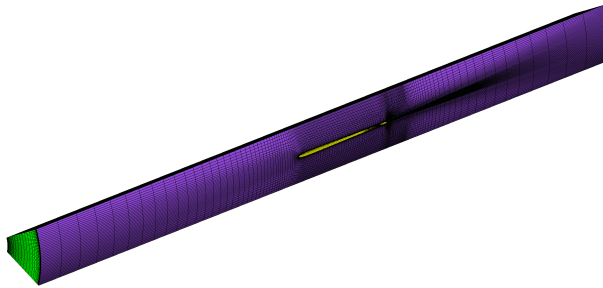


**Figure 4.3:** Overview of CFD mesh.

30° angle. The blades were made using a 3D CAD software, and manipulated in order to import into a meshing software. Small features, i.e. bolts and holes, and the pockets for the strain gauge sensors were filled in order to simplify the model.

The mesh was created in ANSYS Turbogrid, which automatically creates a high-quality structured H-grid mesh, consisting of hexahedral elements. To use this tool, one can either define a geometry by use of CAD or profile points. This thesis used profile points, by creating curve points for the hub, shroud, and blade profile. The curve files contain coordinate points that define the aforementioned geometries. Configurations of one and eight blades have been created, where the one blade configuration use axisymmet-

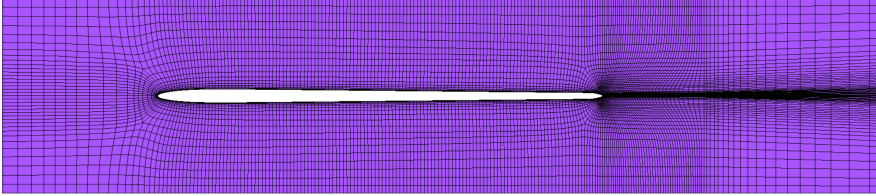


**Figure 4.4:** Close-up image of blade passage.

ric cyclic symmetry, represented as periodic boundary condition, allowing for significantly lower number of elements and computational time. Only the one-way FSI damping simulations were carried out using this periodic interface condition, whilst the rest use the full eight-blade configuration. Turbogrid produce a mesh for one flow passage in a radial blade cascade, as shown in figure 4.3.

To reduce errors propagating from poor boundary conditions, the length of the domain was made long without using too many elements. It is recommended that the length from leading edge to inlet, is at least 10 times the pipe diameter [16]. This is to maintain a developed velocity profile which corresponds to the set inlet boundary condition. This was however not done, as it meant a greater number of elements, thus greater computational time and poor element quality. The length from trailing edge to outlet is also required to be long enough to capture the behaviour at the wake. In a turbulent flow, physical variables vary the most around the boundary layer. This is why it is important with a fine mesh near this region, to capture the physics. The  $y^+$  in the wake region is in the interval of 21.2 to 22.3, 22 by the trailing edge at hub and shroud sides, and maximum 95 at the leading edge by the hub. This means the viscous sub-layer is not fully resolved as this requires a  $y^+ = 1$ . The values mentioned indicate the flow is in the buffer layer and log-law region, where both viscous and turbulent stresses are of similar magnitude. This may be regarded as a source of numerical error. However, this is a fine balance between computational time and low  $y^+$  value. A mesh which fully resolves the viscous layer would potentially result in extended computational time, whilst also increase the risk of mesh folding when conducting two-way FSI simulations. Length from the inlet to the leading edge of the blades was set to 771.4 mm and 836 mm downstream from trailing edge to the outlet, such that the total domain is 1607.4 mm

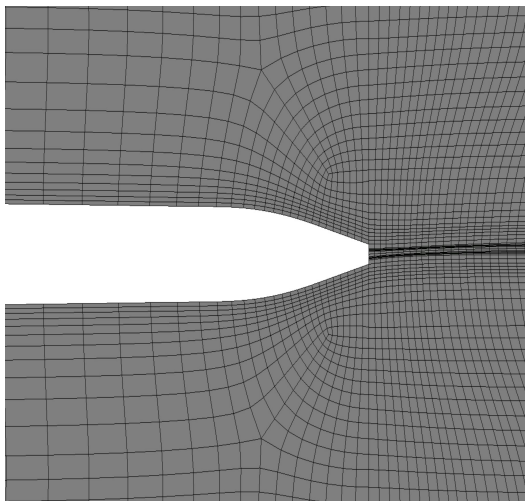


**Figure 4.5:** Mesh zoomed in at trailing edge.

long from inlet to outlet.

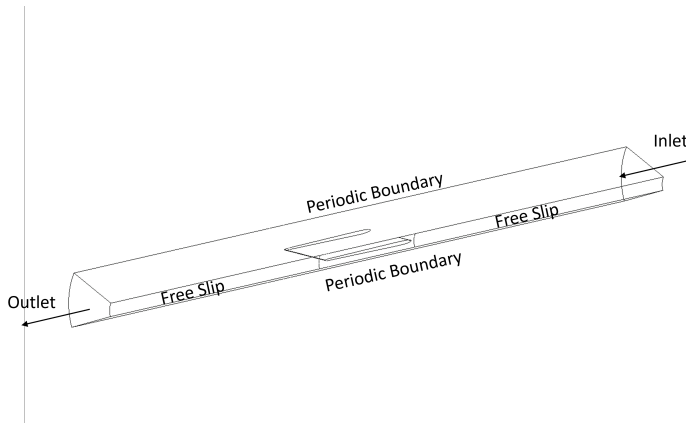
## 4.2 Boundary conditions and mesh discretization study

CFX-Pre was used to set boundary conditions, physical and material properties. For the eight-blade configuration the duplication took place in CFX-Pre, and it was able to both transform and "glue" the mesh such that a conformal mesh was produced. The transient simulations were conducted in order to identify at which velocity oscillations due to vortex shedding would be observed. This would be useful for prescribing boundary conditions for the two-way FSI simulation. Velocities between 2 and 13  $\text{ms}^{-1}$  was tested. In addition to the boundary conditions in table 4.1, a maximum of 3 and minimum of 1 coefficient loops were used. At 13  $\text{ms}^{-1}$ , the Reynolds number is 3 485 600.

The outlet pressure was set to 0 Pa, relative to atmospheric pressure as reference. The wall conditions are set as smooth walls, where the shroud is with the no-slip condition. The hub is different, as only the section where the blades are attached has the no-slip condition. The extended hub surface, upstream and downstream of the blades, is set to a free-slip condition. A turbulence intensity of 5% is used.  $k-\omega$  SST turbulence model is chosen,

**Table 4.1:** Selected boundary conditions and other parameters for the transient simulation.

Parameter	Setting
Transient scheme	Second Order Backward Euler
Advection scheme	High Resolution
Turbulence numerics	First Order
Inlet velocity	$U = [2, 13] \text{ ms}^{-1}$
Outlet pressure	relative pressure: 0 Pa
Turbulence model	$k - \omega$ SST
Convergence criteria (RMS)	$10^{-4}$

**Figure 4.6:** Numerical setup in CFX.

as the steady state simulation was also set to this, and previous numerical investigations, such as Tengs et al. [14]. However, it may be an option to use SST-SAS turbulence model, as this resolves a wider range of turbulent structures in the wake by introducing a length scale equal to that of the vortices downstream. Default wall function were used.

To resolve vortex shedding, a small enough time step must be chosen. It is recommended to use 100 time steps during one vortex shedding period, as recommended in Vu et al. [25]. This also requires a sufficiently fine mesh to capture the shedding. Empirical relations were used to find an estimate for vortex shedding frequency. Firstly is the traditional Strouhal shedding frequency,  $f_s$ . Equation (3.9) is more specific for Francis turbines and it addresses the trailing edge geometry. This present study assumes the Strouhal

**Table 4.2:** Selected time steps for the different velocities.

Velocity [ $\text{ms}^{-1}$ ]	$\Delta t \cdot 10^{-5}$ [s]
2	6.69
4	3.32
6	2.20
8	1.65
9	1.46
10	1.32
11	1.20
12	1.10
13	1.01

number to be  $St = 0.22$ , a commonly used value [26]. In order to have 100 periods of vortex shedding, time steps were chosen for the different inlet velocities. This gives the time step to be determined by  $\frac{1}{100 \cdot f_s}$ .

Root-mean square (RMS) courant number for the numerical domain were kept well below 0, while the maximum was found to be 0.66. On the blades, the largest Courant number was found to be 0.65 at the leading edge and 0.08 just ahead of the trailing edge. As CFX is an implicit solver, it is not required to have a Courant number below 1 for stability.

For the temporal discretization in the transient simulations, a Second Order Backward Euler scheme was used. High resolution was used for the advection scheme and the turbulence numerics. For the advection schemes, the high resolution varies its blend factor between 0 and 1 such that the scheme switches between first order and second order schemes based on the local solution field to enforce boundedness criterion. For high gradient areas, a blend will be closer to first order to prevent undershoots, overshoots and maintain robustness. This may cause numerical diffusion and thus lower accuracy. For low gradient areas, the blend will be closer to second order for accuracy. Turbulence numerics is set to first order.

To determine an estimate of discretization error, a mesh independence study was conducted, in accordance to the guidelines presented in the article "Procedure for Estimation and Reporting of Uncertainty Due to Discretization in CFD Applications" by Celik et al. [1]. This section describes the procedure of the study and the results from it. Mesh independence study was performed on a one-blade configuration in order to save computational time, such that number of elements would be reduced by a factor of 8. Inlet

**Table 4.3:** Table of calculated values from mesh independence study using procedure by Celik et al. [1].

Parameter	Max. streamwise velocity
$N_1, N_2, N_3$	983 339, 402 004, 169 332
$h_1, h_2, h_3$	2.038, 2.746, 3.6629
$r_{21}$	1.347
$r_{32}$	1.334
$\phi_1$	6.623
$\phi_2$	6.635
$\phi_3$	6.641
$\phi_{32}$	6.6286
$\phi_{21}$	6.6106
$p$	2.235
$GCI_{32}$	0.00001%
$GCI_{21}$	0.00009%

velocity was set to  $6 \text{ ms}^{-1}$  and outlet pressure was 0 Pa. As the article describes, three significantly different meshes are to be selected and simulations to be run on them. Taking the initial mesh as coarse, a medium and fine mesh was created. This was done by adjusting the global growth rate factor in ANSYS Turbogrid. It is recommended to use a refinement factor of 1.5, however a factor of 1.3 was considered sufficient.

The meshes are referred to as 1, 2 and 3 for the fine, medium and coarse mesh respectively.  $N$  is denoted as number of elements,  $r$  is the refinement factor,  $\phi$  is the variable of interest,  $p$  is the apparent order of the method.  $\phi_{ext}$  is the extrapolated variable of interest,  $e_a$  is approximated error, and  $GCI$  denotes the grid convergence index.

It is important to choose a variable which captures critical aspects of the physics and considered significant to the simulation study, and is commonly seen in literature. This is chosen as the spatially averaged velocity profile in the wake. The velocity profiles were obtained by averaging the streamwise velocity  $w$  at the position  $z = 0.15 \text{ mm}$  downstream of the trailing edge.

Both  $GCI$  percentages are very low, which suggests there is little to be gained by choosing the finer mesh. The extrapolated values of  $\phi$  suggest that the finest mesh should be chosen. However, the difference in extrapolated and calculated values are assumed to be of little significance, such that the medium mesh was deemed appropriate to use. Furthermore, the apparent

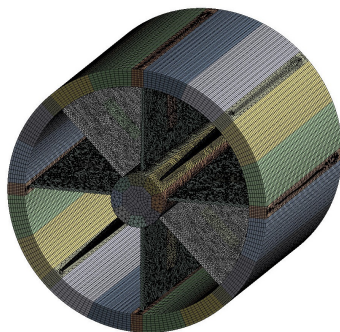


**Figure 4.7:** Mesh model used in FEM solver.

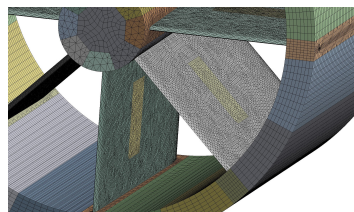


**Figure 4.8:** Zoomed in on piezoelectric patch.

order,  $p$  is at 2.235. Ideally, this should be around 1.5 for CFX, though it may be argued that the calculated  $p$  is still a reasonable value.

### 4.3 Structural model

The structural domain consists of 8 hydrofoils, a hub, a shroud and piezoelectric patches placed on both surfaces of each blade. There are no bolts connecting the hydrofoils to the hub, such that it is held in place by tension as the blades are slid and fit into place. Moreover, strain gauges are placed near the trailing edge and leading edge as the stress is expected to be greatest. These sensors are neglected in the numerical model used in this thesis. The mesh consists of 1 533 054 nodes and a global element size of 12 mm. The core of the hub consists of hexahedral elements whilst the part connected to the hydrofoils consists of tetrahedral elements and is set to be minimum 5 mm. The shroud consists of hexahedral elements only and have the minimum and maximum element size set to 5 and 12 mm. The model has hexahedral elements in an attempt to reduce computational resources. This is done by using MultiZone, as this uses an algorithm to partition the geometry such that a structured hexahedral mesh is generated. The hydrofoils are set to 4 mm, while regions close to the hub, shroud and piezo patch is set to 3 mm. Moreover, the trailing edge have smaller element sizes as these are high stress areas. The piezo patches have an element sizing of 3 mm. With 4 degrees of freedom at each node, there are 6 132 216 degrees of freedom in total.



**Table 4.4:** Table of material properties for the piezoelectric material.

Parameter	Notation	Value
Density [ $\text{kg}^3\text{m}^{-3}$ ]	$\rho$	7800
Relative permittivity at constant strain [-]	$\epsilon_{11} = \epsilon_{22}$	926
	$\epsilon_{33}$	794
Young's moduli [MPa]	$E_1 = E_2$	62344
	$E_3$	52438
Shear moduli [MPa]	$G_{13} = G_{23}$	21295
	$G_{12}$	23020
Poisson's ratio [-]	$\nu_{13} = \nu_{23}$	0.46
	$\nu_{12}$	0.35
Piezoelectric strain coefficients [ $\text{m V}^{-1}$ ]	$d_{31}$	-1.909E-10
	$d_{33}$	4.085E-10
	$d_{15}$	5.731E-10

Piezoelectric patches consist of several layers, such as electrode, piezoceramic layer and insulators. However, the MFC patches have been modelled as single layer in Ansys's FEM solver. It is assumed as a homogeneous piezoelectric material. The piezoelectric patches are modelled with a tetrahedral mesh and the mesh consists of SOLID227 elements. This element type is for tetrahedral elements, and have ten nodes with up to six DOF per node that allows for electromechanical coupling. For piezoelectric simulations, three DOFs are for displacement in x, y, and z direction whilst the fourth DOF is voltage. As also observed in the table 4.4 , the material properties are the same along the x and y axis. A voltage may be applied to one of the flat surfaces while the other is grounded. This allows for the polarization vector to be normal to the blades. In the experimental setup, these patches are glued in place using epoxy glue. The model used for this paper neglects epoxy glue and uses a model with a cavity in the hydrofoil where the piezo patches are placed inside.

As the material is not a part of the standard library of materials, material properties were defined using a script of commands, which is shown in Appendix C. Relative permittivity is defined under constant strain, Young's moduli, Shear moduli, Poisson's ratio and strain coefficients are defined for all directions of the piezoelectric patch.

## 4.4 Modal analysis and harmonic response

For the modal and harmonic analysis, fixed supports and the material was set similarly to the structural analysis. No pre-stress is used. For the solver type, the PCG Block Lanczos method is used to solve the symmetric eigenvalue problem at hand, as it is commonly used for very large symmetric problems containing more than 500 000 degrees of freedom [27]. The modal analysis was limited to find 41 modes, such that this yields up to 5 eigenmodes and its different Nodal Diameters. The modal analysis does not need a load as it only solves the eigenvalues and eigenmodes.

The harmonic response does require a load, which is where the piezoelectric patches are excited. The piezoelectric patches are excited using MAPDL code appended in appendix. A frequency sweep is done at the range 1600 Hz to 4200 Hz, based on results of the modal analysis. This allows for an investigation of the frequency response at the proximity of significant eigenfrequencies, using harmonic response analysis. It is also important to stress the necessity of considering the phase angle, as this is also a requirement for the resonance phenomena. For the harmonic response, the mode superposition method is applied as only a frequency varying load is applied [27] and modal decomposition is used to reduce computational effort [14]. Moreover, sine/cosine mode shapes are observed in pairs such that the eigenfrequencies nearly coincide with each other, but with different positions for the nodes for different pairs.

## 4.5 Acoustic model

The acoustic model neglects the shroud, and in place includes an enclosure which represents the water that is in contact with the blades and thus inside the test section. This acoustic domain is set to be 1.4 times longer than chord length in flow direction. The density and speed of sound in water are the necessary parameters, as seen in equation (3.49). A fixed constraint is placed on the shroud-end of the hydrofoil. A fluid-solid interface is used to ensure shared nodes at where the fluid and structure is in contact. A similar mesh strategy is used for the acoustic model as for the model without acoustic elements. The enclosure that consists of tetrahedral elements only and has an element size of 12 mm. The total number of nodes is 945 258 and the global element size is set to 8 mm. The hydrofoil and piezo patch are set to 4 mm. Moreover, the solver type is set to fully damped due to the surrounding water. The number of degrees of freedom is four at each node,

which gives 3 781 032 degrees of freedom.

The acoustic modal and harmonic response analysis use a similar model as to the analysis done in air. However, as mentioned above, the shroud is substituted with fixed constraint and enclosure. This problem now becomes an unsymmetric eigenvalue problem due to the coupling of acoustic and structural. The full damped method is used to calculate the mode shapes and its frequencies as damping effects due to the surrounding water is of interest. This was set by default by using Ansys Workbench, however, it is also possible to use QR damped method that is faster and more efficient in calculating than the damped method [27]. For the harmonic response, a full harmonic analysis method is used as it accommodates for unsymmetric matrices. Variational Technology is set to program controlled, such that the most efficient method is chosen.

## 4.6 Mesh dependency test

A mesh dependency test was conducted for the structural models, one for with and without an acoustic domain. Five meshes with increasing number of nodes were used, and the eigenfrequency was the parameter of choice as this is mesh sensitive. A strict procedure was not followed as for the CFD mesh. This was mainly because the meshing strategy did not allow for an easy adjustment of number of nodes as several parameters were adjusted to increase or decrease the number of nodes. For the model without acoustic elements, one can see a slight improvement for the medium coarse mesh and the finest mesh, where an increase of approximately 0.11% is seen. This justifies the use of a medium coarse mesh, which consists of 1 113 857 nodes.

This is the case for the model with acoustic elements too. While increasing the node count, the natural frequencies seem to converge to one value, indicating that the values are mesh independent. This may be seen in figure 4.10. However, as there is only a slight discrepancy of 0.15% to the finest mesh, the the medium coarse mesh is chosen, consisting of 898 524 nodes.

## 4.7 FSI setup

For a FSI simulation, the deformation of the flow field is a problem that needs to be considered. Pressure loads due to the flow results in deformations

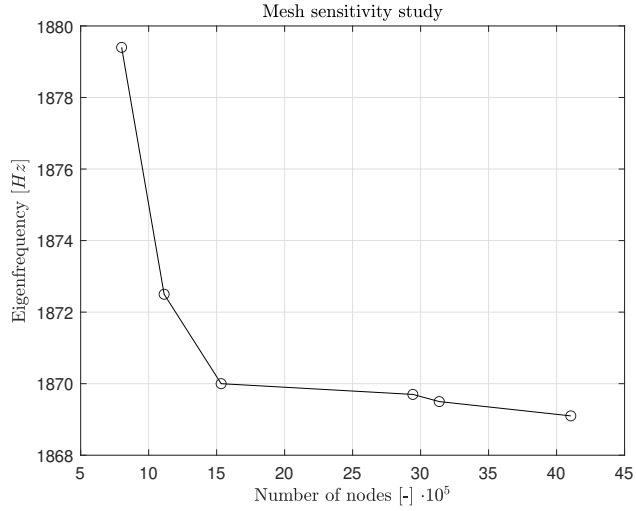


**Figure 4.9:** Mesh dependency test in air

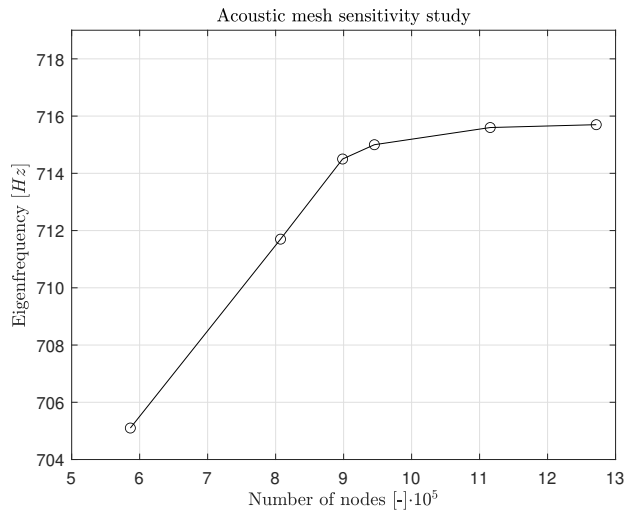


**Figure 4.10:** Mesh dependency test in water

on the blades that the CFD mesh must adapt to. Both a sufficient numerical mesh and mesh stiffness is required to compute the mesh displacements. This is relevant for both one-way FSI and two-way FSI simulations, where mesh motion is involved. With vortex shedding and especially the lock-in phenomena, it represents a strong coupling between the mentioned fields, where the structural deflection may be the dominant factor in the shedding mechanism.

In a CFD analysis, boundaries are stationary such that this must be specified in CFX [28]. This is done by setting the ‘Mesh Deformation’ option in CFX to ‘Region of Motion Specified’, so that the CFD mesh may adapt to the deflections that are transferred from the structural domain. Mesh motion is handled by a model called ‘Displacement diffusion’ which diffuses the displacement of the boundaries onto mesh nodes as:

$$\nabla \cdot (\Gamma_{disp} \Delta \delta) = 0 \quad (4.1)$$

$\Gamma_{disp}$  is the mesh stiffness,  $\delta$  is the relative displacement relative to previous mesh location. This equation is solved at the start of each time step. Mesh stiffness is case sensitive variable that needs to be tuned. Regions of interest, such as the boundary layer and the trailing edge more specifically, require high stiffness as this is where the mesh displacement may be high. Small cell volumes, such as inflation layers in the boundary layer, or cells with aspect ratio are sensitive to mesh deformations. There are four options, where two of them are ”increase near small volumes” and ”increase near boundaries”. Another option is a blend between these, and a fourth option is a specific value of mesh stiffness. Increase near small volumes lets cells with larger control volumes absorb more mesh motion such that the sensitive small volumes are not deformed, and no additional equations are required. Increase near boundaries increase the stiffness near boundaries such as inlet, outlet, walls such that the interior mesh will absorb more mesh motion. However, this does require an additional equation to be solved. For both these two options, a stiffness coefficient  $C_{stiff}$  is used and an increase results in an exponential increase in the rate of stiffness across the mesh. By default it is set to 2. Blended distance and small volumes option is case adaptive which reduced the need for tuning as it combines the two options using weight factors. Moreover, a mean control volume is used to calculate the stiffness.

**Table 4.5:** Selected boundary conditions and other parameters for the transient one-way FSI

Parameter	Setting
Transient scheme	Second Order Backward Euler
Advection scheme	High Resolution
Turbulence numerics	First Order
Inlet velocity	$U = 13 \text{ ms}^{-1}$
Outlet pressure	relative pressure: 0 Pa
Turbulence model	$k - \omega$ SST
Convergence criteria (RMS)	$10^{-4}$
Stiffness coefficient	2
Time step size, $\Delta t$	$5.335 \cdot 10^{-6} \text{ s}$

#### 4.8 One-way FSI: Hydrodynamic damping

The first one-way FSI simulation is to determine the damping effects due to the presence of water. Using modal analysis, the mode shapes and the oscillatory motion may be prescribed onto the blades in CFX as a mesh motion with periodic displacement. CFX is used to determine the work done by the blade on the surrounding water whilst modal analysis provides the rest of the information. Moreover, the maximum deflection amplitude was set in advance to 0.02% of blade chord length, i.e 0.054 mm as the chord length. This was necessary to prescribe the motion in CFX. Work is calculated within CFX by using an built-in feature called aerodynamic damping monitor, by combining and discretizing equations (3.46) and (3.47). This monitors the integral above that is normalized by  $2\pi\omega^2 q_0^2$  [28]. Moreover, this is carried out for 100 periods to reduce uncertainties. A transient blade row setup is required to use aerodynamic damping monitor. To diffuse the mesh deformation, the displacement is set to be relative to initial mesh and mesh stiffness option to increase near small volumes with a default stiffness coefficient,  $C_{stiff} = 2$ .

The time step is based on the eigenfrequency of the blade at 1874.4 Hz, and it is ensured 100 oscillations per period. This gives a time step size

$$\Delta t = \frac{1}{100 \cdot f_{shedding}} = 5.335 \cdot 10^{-6} \text{ s} \quad (4.2)$$

Due to this low time step, the single-blade configuration was used with periodic boundary condition in order to ease the computational costs. In addition to solving the fluid flow equations, mesh displacement is involved such

that it is more demanding to solve. The simulation was initialized with a converged transient simulation at a time step of  $\Delta t = 1 \cdot 10^{-5}$ s. This was to minimize transient start up errors, such as backflow near the outlet, which would result in a simulation crash. The RMS Courant number is 0.06 and max at 0.47.

## 4.9 Two-way FSI

A two-way FSI analysis was conducted using Ansys CFX and Ansys Mechanical coupled through System Coupling. In Mechanical, the FSI-interface is defined in the model, while the blade surfaces are defined in CFX such that System Coupling may recognize this. Furthermore, in CFX-Pre, the mesh motion of the blades are defined by the deformation calculated and transferred from Ansys Mechanical. The deformations are thought to seize control of the shedding mechanism, similarly to the one-way FSI simulation but not to the same extent as the oscillation frequency is lower.

A two-way FSI is known to be very unstable. As mesh deforms, the elements of high aspect ratio or small control volume may be significantly deformed resulting in a negative cell volume. This results in mesh folding and the CFD-solver to crash. This may be worsened by the onset of a presumed vortex shedding, as in the one-way FSI simulation. By tuning the stiffness coefficient and Under Relaxation Factor (URF), a simulation crash may be prevented or delayed. As mentioned previously, increased stiffness coefficient increases the rate at which stiffness is distributed over the mesh and thus the diffusion of deformation [28]. URF is commonly applied on forces, and partitions the force distribution that is transferred between CFX and Mechanical. This is to give the mesh more time to adapt to the deformation by applying an interpolated force. Assume a load  $\Phi_i^n$  at time step  $n$  and cell  $i$ . The updated load  $\Phi_i^{n+\frac{1}{2}}$  will then be:

$$\Phi_i^{n+\frac{1}{2}} = \Phi_i^0 + \alpha(\Phi_i^{n+1} - \Phi_i^n) \quad (4.3)$$

where  $\alpha$  is the URF and  $\Phi_i^{n+1}$  is the predicted load at next time step. URF helps with stabilizing the solution but at the cost of convergence time.

From a transient CFD simulations, it was observed that vortex shedding was observed at a frequency of 199.6 Hz, although hand calculations calculated the 5th harmonic frequency. The amplitudes corresponding to the first harmonic was significantly higher than the other harmonics and so that it is the deciding factor for the time step size. Based on the shedding frequency

and ensuring 100 samples per period, a time step was chosen to be:

$$\Delta t = \frac{1}{100 \cdot f_s} = 5 \cdot 10^{-5} \text{ s}. \quad (4.4)$$

To initialize the flow field, a solver input file with a converged transient solution was used to initialize a 2-way FSI simulation with a time step of  $10^{-3}$  until the residuals and monitor values converge. This was then used to initialize a simulation with the time step of  $5 \cdot 10^{-5}$ .



## Results and discussions

*In this chapter, the results are presented in the same order as how the numerical methods section was set up: transient CFD simulations, modal and harmonic response analysis, followed by one-way and two-way FSI. The CFD simulations were presumed to exhibit vortex shedding and this velocity was used for the FSI simulations. Modal analysis showed eigenfrequencies and mode shapes, which was used in the one-way FSI and for the harmonic response analysis. This harmonic response used piezoelectric patches to excite the blades at desired frequencies to investigate the deformations. Lastly, results from the FSI simulations are discussed, before a comparison on flow fields is made.*

### 5.1 Unsteady CFD simulations

In order to run a two-way FSI simulations, several transient CFD simulations were run for varying velocities to see which result in vortex shedding to be observed. At  $13 \text{ ms}^{-1}$ , the monitor points placed 15 mm downstream of trailing edge exhibited oscillations for velocity and pressure whilst the normal force on the blade in perpendicular direction showed similar frequency of oscillations. However, at lower velocities, this was not the case. The normal force on the blade oscillated given enough time while pressure and velocity did not oscillate, suggesting no vortex shedding present.

FFT was used on the fluctuating monitored values to identify which frequencies were dominant and at which amplitudes. Several harmonics were observed, where the first at 199.9 Hz gave the largest amplitude, albeit an amplitude of only 0.49 Pa. Two other harmonics were observed as 2nd and 4th harmonics, at 396.5 Hz and 789.9 Hz corresponding to amplitudes of

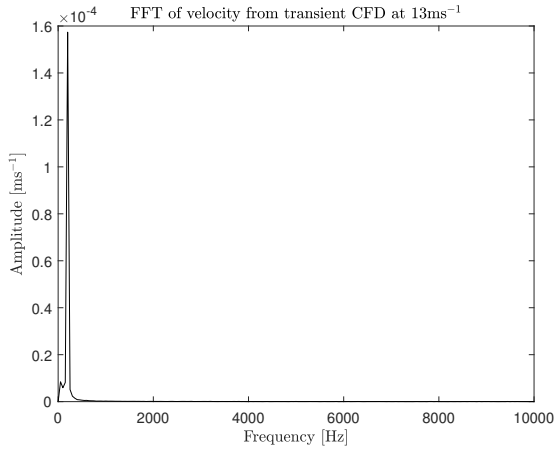


**Figure 5.1:** FFT of velocity fluctuations showing

$1.82 \cdot 10^{-2}$  Pa and  $9.5 \cdot 10^{-3}$  Pa. The Strouhal shedding frequency relation predicted a shedding frequency of 752.4 Hz. This seems to have estimated the 4th harmonic, with a deviation of 4.7%. Brekke's empirical formula (3.9) was more accurate at estimating a frequency of 989.7 Hz, which seems to be the 5th harmonic with deviation of only 0.02%.

Although there was a match between the estimated shedding frequencies using empirical equations, and the harmonics of the shedding frequency from CFD simulation, the amplitudes were very low. Therefore it was necessary to further post-process these results. CFD-Post was used to visualize regions where vortex core are present in the flow field. Albeit the vortex structures can be captured and visualized, they are only qualitative such that there are no outputs of numerical quantities. There are several ways to this, but this case a Vortex Core Region 'Location' is used with the Q-criterion as the method. The method is case sensitive such that this thesis has picked the one which shows the vortex structures clearly. The Q-criterion is described as the second invariant of the velocity gradient tensor.  $Q$  is defined as

$$Q = \frac{1}{2} \|\Omega\|^2 - \|S\|^2 \quad (5.1)$$

where  $\Omega$  and  $S$  are the antisymmetric and symmetric components representing rates of rotation and strain [29]. This seems to filter out vortex structures that may arise due to the strain tensors near the boundary layers of the walls and blades. A vortical structure may be observed just downstream of the

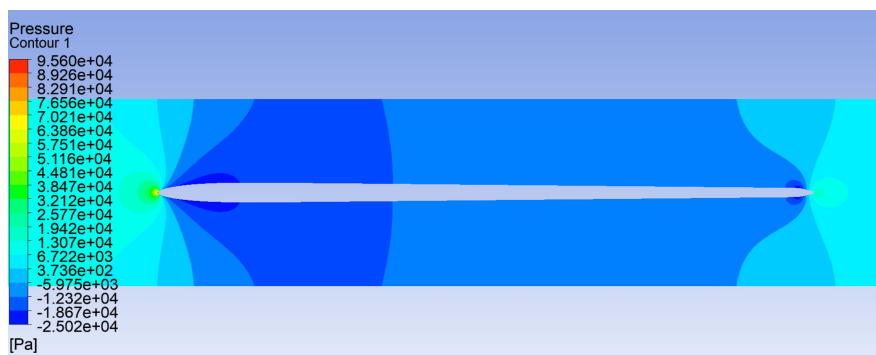


**Figure 5.2:** Pressure contour showing stagnation points and separation points.

trailing edge, mid-way of the span of the blade in figure 5.3 for  $Q = 0$ . These structures do not resemble von Karmán vortex street that have the characteristic alternating structures. There seems to be two structures on each side. A possible cause is that the mesh is not refined well enough to capture each alternating structure, such that it has been diffused, or blended into a single structure instead of alternating structures. As mentioned in chapter 4.1, the mesh was optimized given time constraints and computational resources. Therefore, a too fine mesh would be too demanding for FSI simulations.

One can also argue that the observed structures and the oscillating monitor values are due to a numerical instability that arise at a high enough velocity. Near the boundary layer and walls, mesh elements have high aspect ratio. Another plausible is that that flow is separated near trailing edge and the vortex cores dissipate quickly, such that the structures blend together. Heskestad and Olberts [11] observed similar behaviour for the corresponding trailing edge shape in their experimental work. This was explained by a delayed separation of the shear layers, such that the separation point is near the trailing edge inclination. Further, it was stated that due to separation points being close to each other, their respective velocity fields overlap and destroy each other. Translating this into practice, this means vortex shedding has been avoided, which is a favourable outcome.

Moreover, it may be observed vortical structures that resemble horseshoe vortices near the hub and shroud at the two trailing edge sides, though this is more clearly seen at the shroud side. There is also the possibility that it is not horseshoe vortices but rather discrepancies from the mesh due to the transition between small cell regions and large cell regions.

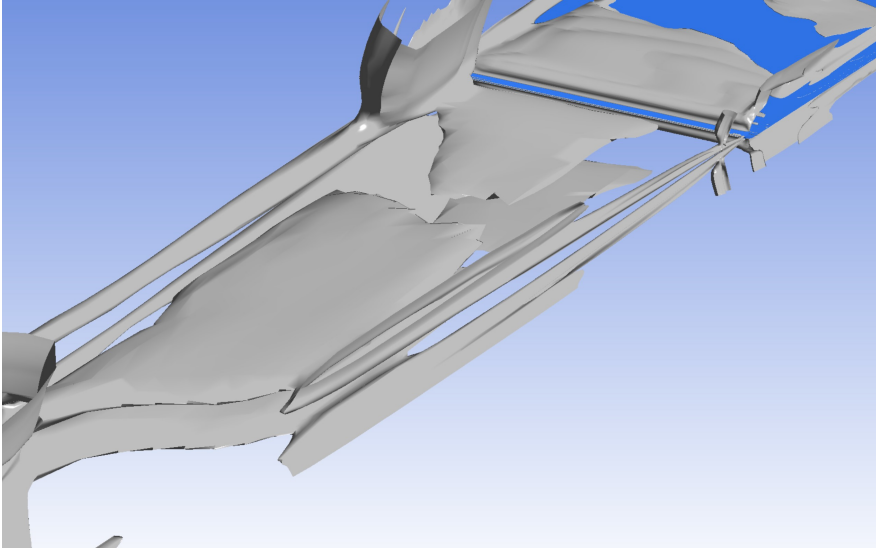


**Figure 5.3:** Isosurface of vortical structures identified by Q-criterion method. No von Kármán vortex street is present.

The pressure distribution is similar for the the transient and steady state simulations. A stagnation pressure is clearly exhibited at the leading edge at a magnitude of 95.6 kPa. The areas of high magnitude of pressure seem to be dominantly on the leading edge side, which is expected. Moreover, a negative pressure gradient can be observed near the point of separation close to the trailing edge, and vortex cores can be identified at this point of separation.

In order to eliminate the argument of a too coarse mesh, an unsteady CFD simulation was run using one blade and periodic interfaces, with number of elements to be 2.2 million, which is roughly 5.5 times more than what was used previously. However similar vortical structures were observed such that it may be fair to state that no vortex structures are observed for the range of velocities tested. Returning to the two possible causes, it seems it is more likely for the oscillating monitor values to arise due to numerical instabilities at the given velocity.

Nonetheless, it is interesting to see why an instability was present at  $13 \text{ ms}^{-1}$ . As there is still some uncertainty to the matter, it is necessary to verify this experimentally.

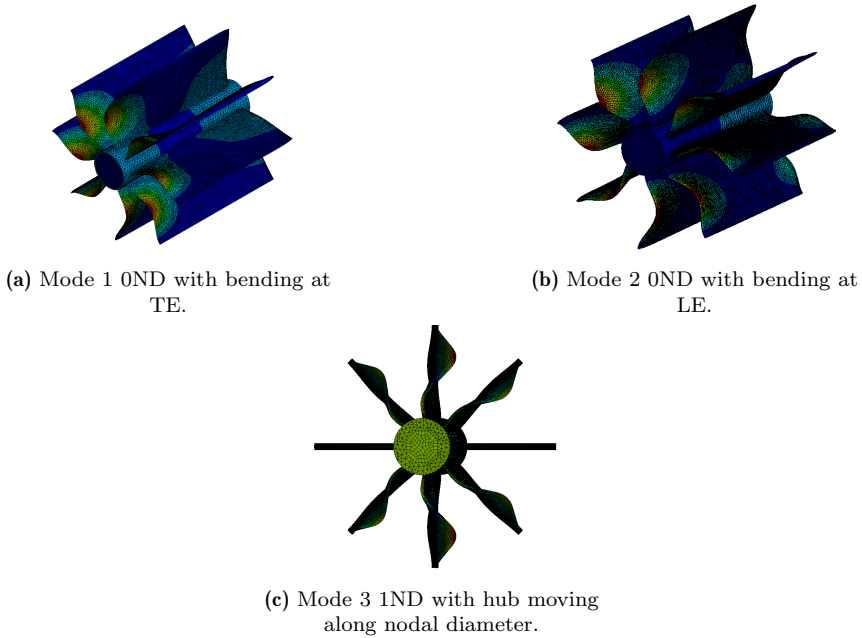


**Figure 5.4:** Mode shapes observed with air.

## 5.2 Modal analysis

The natural frequency of the structure with air was found using modal analysis. Both quantitative and qualitative studies are presented. The displacement in modal analysis is not a true value, but rather an indication of which eigenmodes that may yield the greatest displacements. The shapes are seen in figure 5.4 and 5.5. The most common and studied mode shape is the first bending mode, usually found as the first mode. This is a bending of the trailing edge, which is where the fatigue cracks tend to form over long exposure to cyclic stresses [14]. However, up to 5 modes have been investigated as the requirement for resonance phenomena is both frequency and phase angle. As mentioned in 3, pairs of mode shapes, with different modal position, can be described as the sine-mode and cosine-mode.

First mode is a bending mode at the trailing edge, observed at 1699 Hz at 0ND and the blades bend in the same direction. There is a slight rotation at the hub in z-axis direction, such that a deformation is also present at leading edge. 3 pairs of sine/cosine modes are observed representing 1ND,

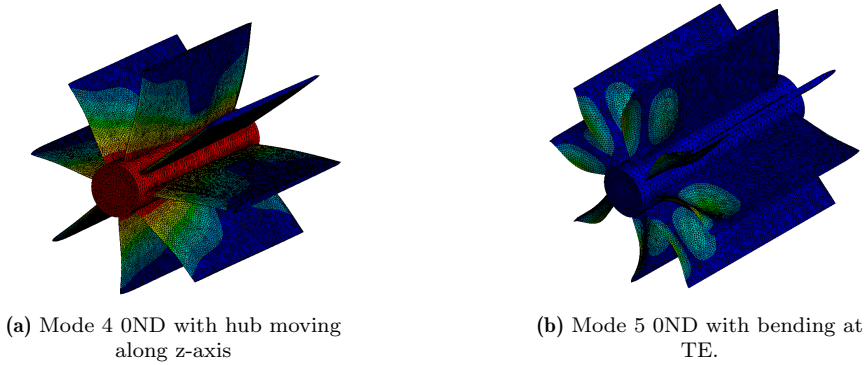


**Figure 5.5:** Mode shapes observed with air.

2ND and 3ND, where the two neighboring blades are bending towards each other. Finally, the last ND of the first mode is similar to the 0ND where there is some rotation at the hub. This too gives a slight deformation at the leading edge, and is observed at 1980.6 Hz.

Next mode shape observed is a pair of the second eigenmode but for 1ND, at 2881.5 Hz. The bending has shifted to the leading edge and bending in the same direction. 2ND mode shapes are not bending in the same direction, but it is also observed slight deformation at one of the blades that supposedly is a node. This could be due to a numerical error that was not considered when conducting the sensitivity test. Moving further in the frequency range for the second eigenmode, a triplet is observed at 2939 Hz. At 3151.1 Hz, the first 0ND is observed with a rotation of the hub, again at z-axis, and a slight deformation at the trailing edge. Moving on, the next observed mode shape is a 1ND at 3661.3 Hz where the hub is flexed in the direction of the nodal diameter and deformation is at the trailing edge. Only the part of the hub near the trailing edge is flexed. This results in 2 half-waves deformation shape, especially at the hub's most flexed position. The fourth observed mode shape is similar to the third, with the hub flexed in the direction of the normal diameter but the largest amplitudes are now observed at the leading edge.

The fifth eigenmode observed is a single mode where the hub is moving in z-axis direction such that the largest deformation is along the hub. This is observed at 4076 Hz.

The acoustic modal analysis shows a first mode as a bending mode at

the trailing edge, where 0ND at 700.7 Hz, shows the bending of blades to be opposite in direction, compared to neighboring blades. Two sine/cosine pairs are observed at 1ND and 2ND respectively where the deflection is in the opposing directions. The final sine/cosine pair is of 1ND and deflections in the same direction. Finally, 0ND is observed again at 885.6 Hz where the blades are deflected in the same direction.

The acoustic modal analysis is expected to report lower frequencies as hydrodynamic damping is now considered. This was also observed in [13], however the numerically obtained frequency reduction ratio (FRF) reported was higher than found in literature. Comparing the 0ND of first eigenmode, a FRR of 0.59 is found.

The pattern of deflection of blades was observed for investigated modes - first 0ND and two sine/cosine pairs deflected in opposite to neighboring blades whilst the last pair and final 0ND have blades deflected in the same direction. The deflection in opposite directions is a pattern that is not observed in Francis turbines, which raises a question of whether this is a numerical error, or if this is coupled to a limitation in the simplification of the sine/cosine blade shape of a Francis turbine blade.

The second mode shape is a bending mode at the leading edge where the zeroth nodal diameter is observed at 1141 Hz. The second 0ND, is observed after the first 2 sine/cosine pairs, which is different to what was seen in the first mode. Here, there is also a rotation of the hub such that there are 2 half-waves at the leading edge. Finally a sine/cosine pair is seen observed. Moreover, this mode is also observed with air but only one 0ND was observed with air. Considering the 0ND of second modes in water and with air, a FRR of 0.6 is observed.

The third eigenmode is observed at 1693.2 Hz where there is motion in z-axis direction and greatest deflection at the leading edge. This mode shape is observed with air as well, but was observed as the fifth eigenmode. Comparing this and the fifth mode with air gives a FRR of 0.58.

A fourth eigenmode, ND0, is observed at a frequency at 1910.4 Hz. 3 half waves are observed, while the greatest deflection is at the trailing edge. At 0ND, a rotation at the hub is seen again. Both 1ND and 2ND is observed, but 1ND was difficult to differentiate from 0ND as there was still some, though small, deformation seen on blades acting as nodes. Looking at higher frequencies, it seems to go back to a pair of 1ND, until a 0ND is observed again. Similar to previous 0ND pairs, this last has blades deflecting in the same direction. The hub is also rotating, resulting in a mode shape that

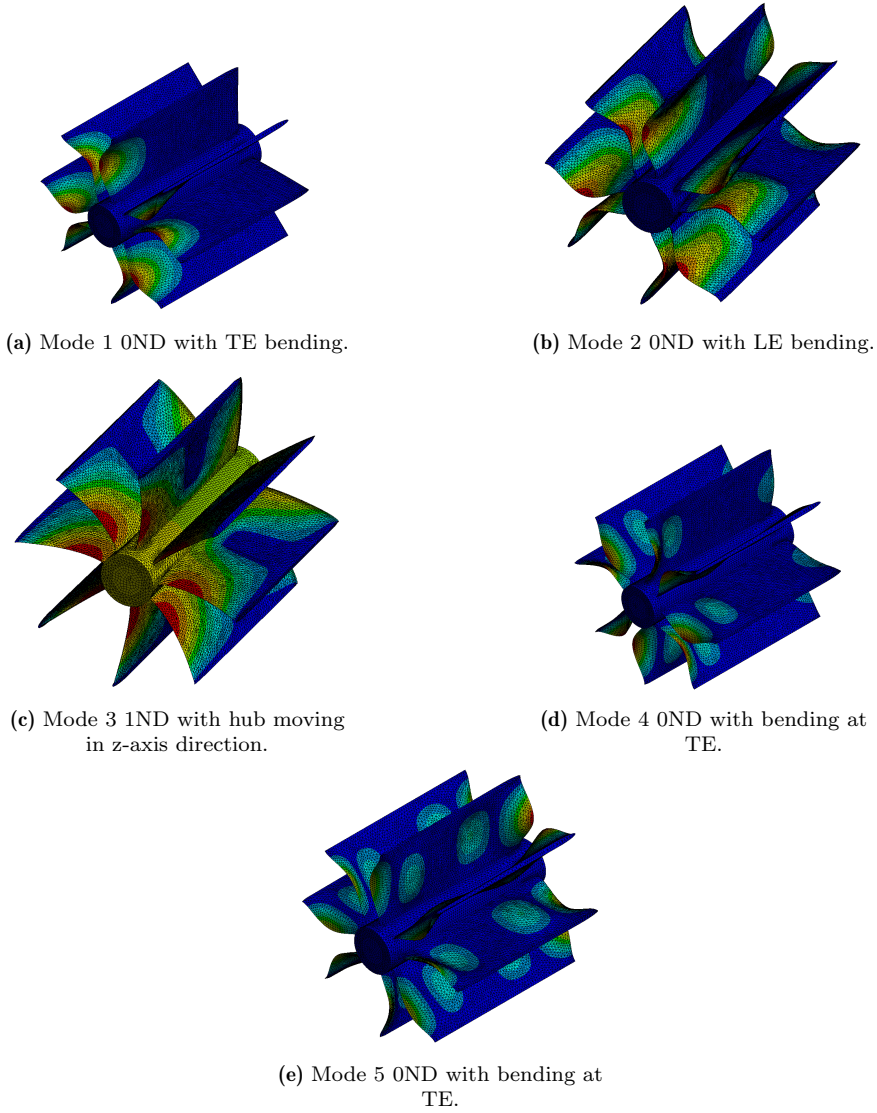


**Figure 5.6:** 5 Mode shapes observed with water



shifts the deformation peaks near the trailing edge. The peak closest to the trailing edge is shifted away, closer to the shroud whilst the other is shifted closer to the hub. This mode shape was not observed for air for the set range of modes investigated and thus it is not appropriate to compare the FRR for this mode.

The fifth and final mode is a mode shape that resembles a cosine curve, across the chord length. The deformation is greatest at leading edge, and 0ND is observed at 2199.2 Hz. However, after one pair of 1ND, another 0ND is observed but the deformation shape is similar to what was observed in the fourth mode, and deflection is greatest at the trailing edge. The mode shape at the next frequency pair is then back to what was observed in the fifth mode. This behaviour was not observed with air.

Different eigenmodes are observed when comparing air and water as the surrounding environment. This is also observed by Bergan et al [9]. The largest difference that was observed was the different order of mode shapes occurring. Secondly, the direction of deflection was different, as for the modal analysis with air showed deflection of blades in same direction. This was only the case for the last pair observed in acoustic modal analysis, except for a few exception such as the axial mode. While a flexion mode was observed with air, where the hub was flexed and moving similar to a pendulum, this mode shape was not found in the range of mode shapes in the acoustic case. This could have been found if the range of modes was extended further. Similar to what was observed in [30], the order of modes found differed for in water and with air. As the frequency increased, classifying the mode shapes became more difficult. The shapes became more complex with more half-waves present. This trend applies for both with air and with water.

An uncertainty linked to the mesh could explain the discrepancies found in the complexity of classifying mode shapes and the agreement between with air and in water. Liang et al. performed a mesh sensitivity study on natural frequencies, but for several other mode shapes and nodal diameters. This present study has only looked at 1ND of the bending mode at trailing edge. Although the literature found the different modes to converge well and at similar rates, there were bigger differences for tetrahedral mesh, which is used in the present study.

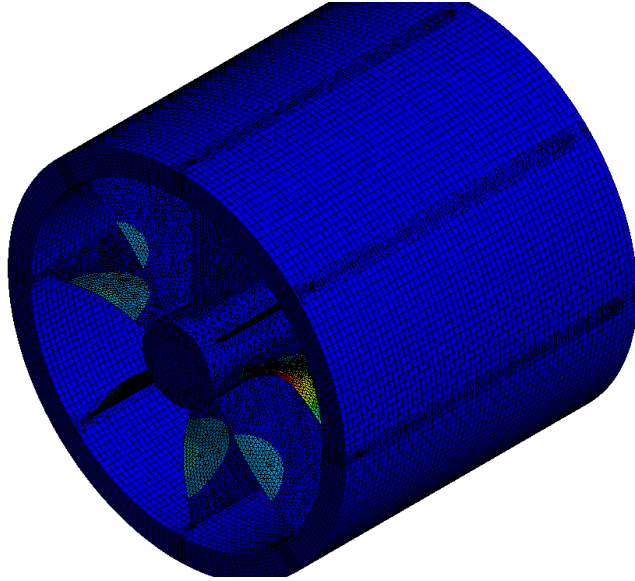


**Figure 5.7:** Total deformation at 1860 Hz and  $-179.6^\circ$ , with no surrounding water.

### 5.3 Harmonic response

A frequency response plot and a phase response plot is produced for the blades. One of each plot is made for each blade. This is because the directional deformation should be relative to the orientation of the blades and not the global coordinate system. However, one frequency and phase response plot is made for all 8 blades together too. For the 8 different frequency response plots, it differs between maximum amplitude at 1860 Hz and 2900 Hz. For the frequency response plot of all 8 blades, it is at 1860 Hz. This frequency and corresponding phase,  $-179.6^\circ$ , is used to calculate total deformation yielding a maximum deflection of  $7.27 \cdot 10^{-3}$  mm. This frequency is in the proximity of the eigenfrequency of first eigenmode, 1ND.

A second critical frequency seems to be at 2900 Hz and  $0.6^\circ$  with a total deformation of  $1.44 \cdot 10^{-3}$  mm, but at the leading edge. This does not seem to be as critical compared to the first eigenmode, which is in agreement of that it is the more important mode shape as often mentioned in literature.

Similar to the harmonic response, frequency responses for both all blades and each blade has been made. The acoustic harmonic response shows that

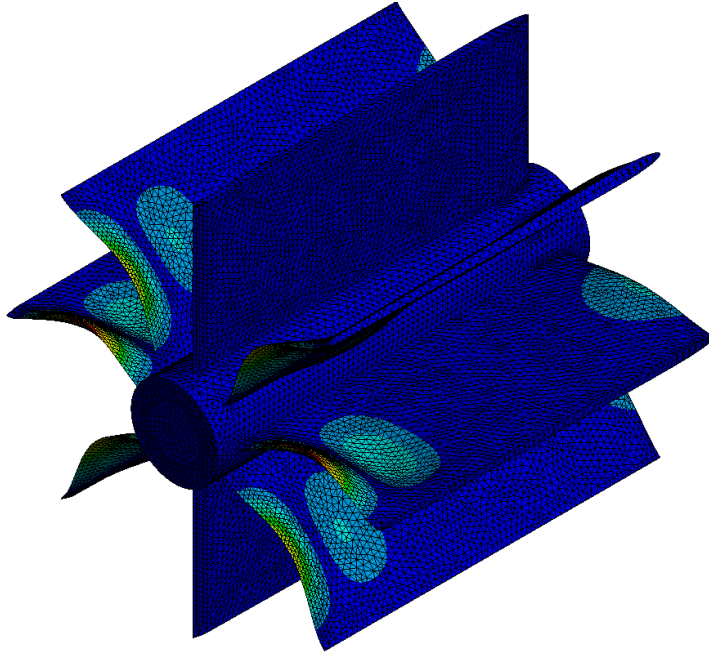


**Figure 5.8:** Total deformation at 2900 Hz and  $0.6^\circ$ , with surrounding water.

the critical eigenmode is in fact the second eigenmode, as the frequency response plot shows the largest peak in deflection and a phase angle of  $-179.8^\circ$ . The total deformation is  $3.55 \cdot 10^{-2}$  mm, which is greater than what is seen with air. The mode shape is the 5th eigenmode with greatest deformations at trailing edge. Another peak was observed, although at a lower amplitude, at 885 Hz corresponding to the first mode shape. This was at an amplitude of  $6.2 \cdot 10^{-3}$  mm. For the case with air, it was the first bending mode that was the critical mode shape and corresponding frequency, but that is not the case for in water. However, it is still a bending at the trailing edge that is deemed critical, which was expected. It is noteworthy that the amplitude response is greater for the submerged case, which initially seems odd. One explanation for this could simply be that fluttering is actually observed rather than damping. Recalling damping vs. fluttering, a positive phase angle indicates that the structure is absorbing energy from the water.

Though harmonic response has been done for small-scale Francis runners and linear blade cascades of similar geometry as present work, the circular

cascade is not found in literature. However, a comparison to numerical analysis done on a model Francis runner shows similar order of magnitude. However, this is not enough to verify the results, but it can be of guidance for experimental work that should be conducted, to investigate if the similar mode shapes and frequencies were found to be critical.

## 5.4 Two-way FSI

Unsteady 2-way FSI is highly unstable, it was necessary to simulate several preliminary simulations to set up simulations properly. However, the small time step resulted in a crash after only a few iterations. This instability was related to the numerical time step size and mesh deformation that gave a negative cell volume. When decreasing the time step, CFX reported 100% back-flow at the outlet, suggesting that either the flow grid was not initialized well or the numerical grid was unable to adapt to the mesh deformation. As described in chapter 3, a large timestep was used to initialize the simulation until a converged solution was attained. Moreover, values for URF, the stiffness of the dynamic mesh and total number of stagger iterations were adjusted to work around the numerical instabilities.

The mapping of the two meshes had a minimum value of 82% and a maximum of 99%. Although the lowest value is in an acceptable value, it may contribute to the problem of displacement to not converging. An acceptable mesh mapping is considered to be around 75%.

The large timestep was based on the 5 samples of one shedding period,  $f_s = 1 \cdot 10^{-3}$ , which is not enough to capture the vortex shedding well. This could be a reason for the simulation to converge well, as the instability was not captured. Moreover, a small timestep leads to an accumulation of errors. As the temporal discretization use a second order accurate scheme, this may reinforce this argument. It was also observed that the data transfer of displacement and its mesh motion struggled to converge. Decreased timestep seems to capture the onset of vortex shedding while also accumulating the discretization errors. This could explain the instability and simulation crash. This onset of instability was reflected in the pressure values monitored 15 mm downstream of trailing edge, as seen in figure 5.9. This may also be observed in contour plots of pressure at two different times, where figure 5.10, shows a converged solution with the stagnation points and separation areas that was also observed in figure 5.1. However, these characteristics are not observed in figure 5.11 such that it is fair to assume the solution has

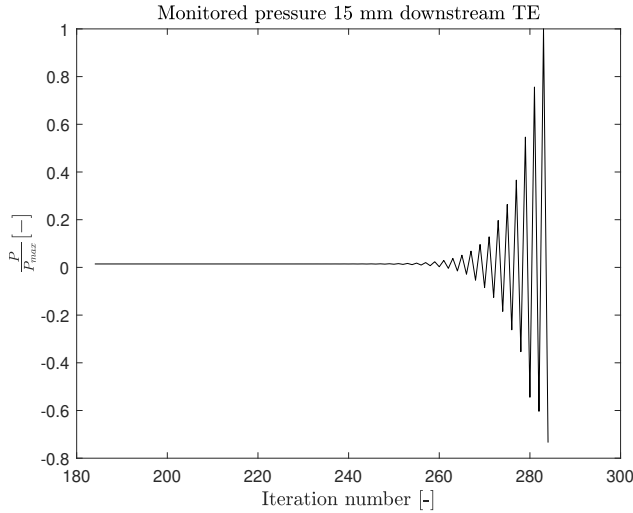


**Figure 5.9:** Monitored pressure 15 mm downstream of TE. Oscillations onset for smallest timestep.

diverged due to the instability, causing the simulation to crash.

The maximum equivalent stress value observed was at the trailing edge at  $1.13 \cdot 10^5$  Pa. A high stress regions is found near the trailing edge close to the hub and shroud, where it was expected to be concentrated. Moreover, it is also observed a relatively high stress region at the mid-span close to the trailing edge. Additionally, the maximum displacement was at the TE mid-span, as expected. This was at a magnitude of  $2.14 \cdot 10^{-7}$  mm. The displacement pattern seem to resemble the first eigenmode that was observed in the modal analysis, which was a bend at the trailing edge.

The model worked well for a timestep of  $10^{-3}$  since the RMS Courant number was constant throughout and stayed at 1.49, while the residuals were oscillating below convergence criteria. Since vortex shedding was not observed for the 2-way FSI simulation, it is fair to assume that this timestep is acceptable, seeing as it showed similar pressure values, pressure field and velocity field to the CFD simulation. CFD mesh is already a structured hexahedral mesh but do not need to be as small in the wake region since vortex shedding is not present. The cells in this region are relatively small compared to the deflection so that instabilities would occur in these regions.

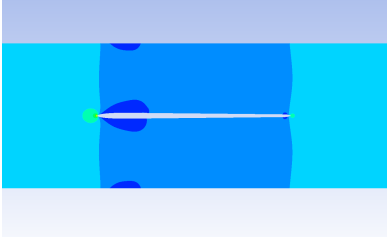


**Figure 5.10:** Pressure contour at time = 0.18035s.  $\Delta t = 10^{-3}$ s.

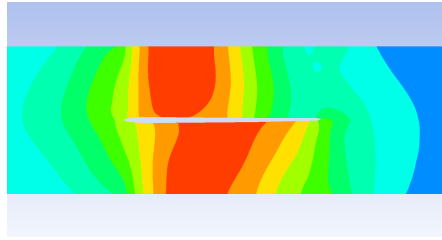


**Figure 5.11:** Pressure contour at time = 0.1852s.  $\Delta t = 5 \cdot 10^{-5}$ s.

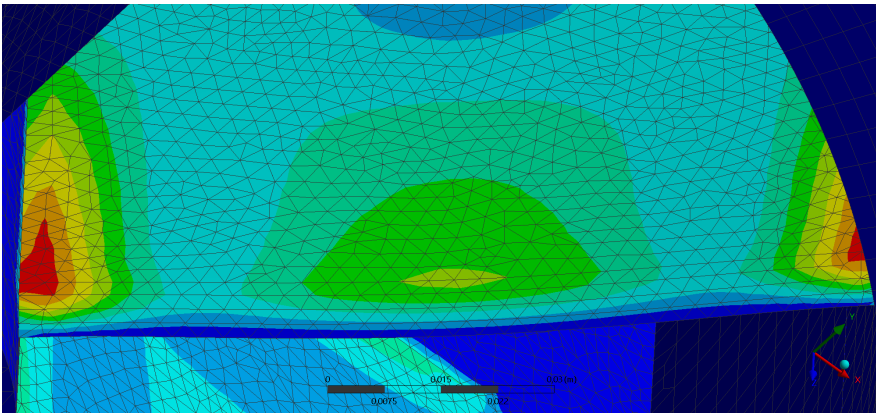


**Figure 5.12:** Maximum stress observed near trailing edge.

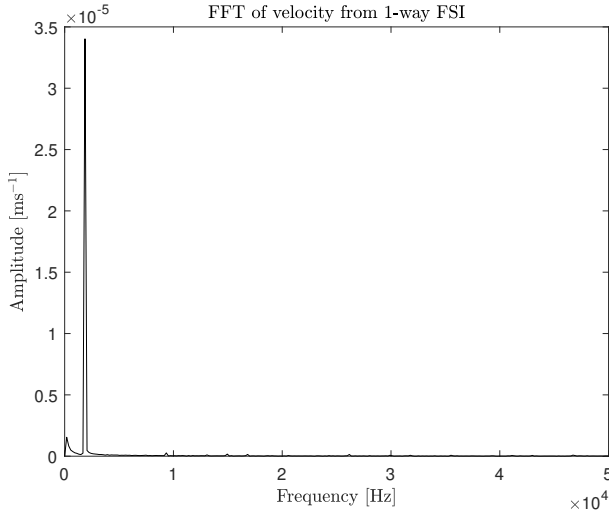


**Figure 5.13:** FFT applied on velocity fluctuations measured 15 mm downstream of trailing edge

## 5.5 One-way FSI

Similar to the two-way FSI, mesh folding was observed but not to the same extent. The instability may be due to the time step as well as it had a much lower time step, at  $1/f_{eigenfrequency}$  and 100 sample periods. The mesh stiffness was modelled with higher stiffness near small volumes and a coefficient of 2. Based on monitor points at the same location as the above cases, a different shedding frequency was observed to what was observed in the unsteady CFD analysis. FFT was applied on these values, as seen in figure 5.13. With a 5.1% deviation, this showed a frequency of 186.9 Hz, a tenth of the frequency prescribed on the blade. This is however at a very small peak, while the largest peak is namely at the prescribed frequency of blade motion with a much larger amplitude. This may suggest that the first peak is only a form of noise, such that the largest peak is actually the first harmonic at which the blade is vibrating at. Furthermore, as seen in figure 5.14 for  $Q = 10^{-5}$ , the vortical structures in the wake of the blade resemble what was observed in the transient CFD simulations. A greater value is used here for  $Q$  than in section 5.1 to reduce noise in form of vortical structures. These structures suggest that despite the structural deformations, vortex shedding is not present. It could be because the deflections are not significant

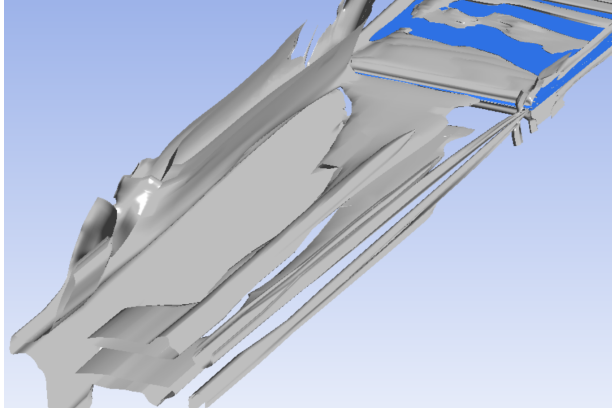


**Figure 5.14:** Q-criterion used to identify vortical structures downstream of trailing edge.

enough provoke vortex shedding, such that the findings of Heskestad and Olberts still applies for the case of a vibrating blade.

Finally, the damping ratio that was showed a ratio of  $\zeta = 2 \cdot 10^{-20}$  which indicates no damping and small vibration amplitude. Looking at this in the context of the results from harmonic response, the deflections are very small. Deflection velocity of the blade is reduced as the deflection is reduced, as blade velocity is given by

$$\dot{q} = \omega q_0 \cos(\omega t). \quad (5.2)$$

This means less work is done by the blade on the surrounding water, such that the damping ratio is as low as calculated. Moreover, the maximum deflection amplitude was tested to see if this had any effect on the damping ratio. Increasing the maximum to 1% of the chord length resulted in a damping ratio in the order of magnitude of  $10^{-17}$  which is greater than for 0.02% of chord length in maximum amplitude, yet still significantly low. There is a possibility that a better model should be made to evaluate the damping ratio.

When comparing to experimental data, this value may be difficult to replicate exactly as an assumed maximum deflection amplitude is set as a constant in the numerical simulation.

Figure 5.15 shows the velocity profiles of the three different cases at 15 mm downstream of the trailing edge, where the length scale has been



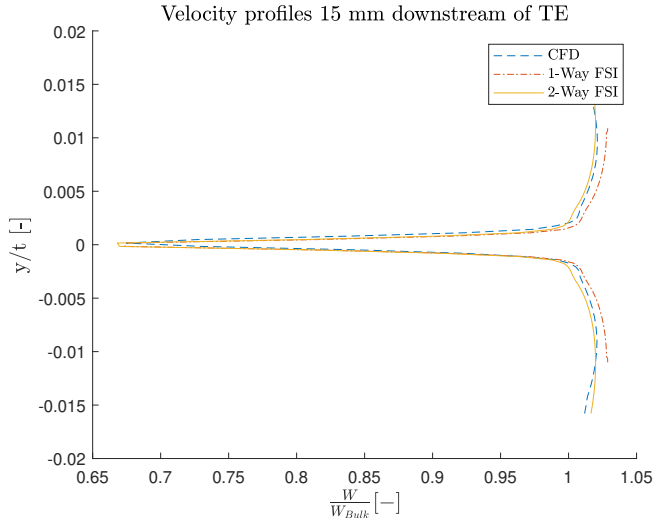


**Figure 5.15:** Velocity profiles 15 mm downstream of TE

non-dimensionalized using trailing edge thickness  $t$  and flow velocity is non-dimensionalized by bulk flow velocity. There seems to be a good agreement between the transient CFD and 2-way FSI simulation but not so much with the 1-way FSI. One reason could be due to the 1-way FSI using only one blade while the other two use a full 8-blade model. Since a periodic interface is used, the other 7 blades are modelled such that there is expected some numerical errors due to this modelling approach. Another reason is that the blade is in fact vibrating, although very small amplitudes, but enough to affect the flow field. Once again, it is interesting to investigate this experimentally to determine if the numerical simulations capture the behaviour.



---

## Chapter 6

---

### Conclusions

In this thesis, CFD simulations were conducted on eight-bladed circular blade cascade to find the lowest velocity with vortex shedding. This was to be used for input parameters for 1-way FSI and 2-way FSI simulations. Moreover, modal and harmonic response analyses were conducted to find eigenfrequency, evaluate the hydrodynamic damping and the response when excited by a piezoelectric patch. 1-way FSI used blade motion from modal analysis.

From the unsteady CFD simulations, pressure fluctuations were observed at monitoring points indicating von Kármán vortex shedding for  $13 \text{ ms}^{-1}$ . However, post-processing showed vortical structures that did not resemble the characteristic alternating pattern of von Kármán vortex shedding. A much finer mesh was tested to investigate whether the mesh was too coarse but yielded similar results. The findings are however in agreement with experimental literature, and is a favourable outcome for designing a Francis runner.

Modal analysis and modal acoustic analysis exhibited similarities in mode shape but also a few different mode shapes for the investigated frequency range. Added mass effect was successfully modelled as there was a favourable FRR. This was expected and also found in literature. However, the FRR done on model Francis runners were lower, but it is uncertain whether it is possible to compare between test rigs and a more complex model, as stated in Liang et al. [13].

A harmonic response analysis was conducted with air and water. The blades were excited using piezoelectric patches. Two different trailing edge bending mode shapes were observed to be critical. A strange observation was made, that the harmonic response in water yielded greater deformation at its

trailing edge compared to in air. This interaction is however not understood properly. Moreover, the phase angle at which the two frequencies varied, as the one with air had a phase angle of  $-179^\circ$  while it was  $179^\circ$  for when submerged in water. This was not in agreement with Liang et al. [13].

One-way FSI simulation used the motion of the first mode shape prescribed onto the blades in the CFD solver to simulate the flow field with a vibrating blade and to calculate damping ratio. FFT analysis on monitor points showed a frequency peak which matched the frequency of the prescribed motion. Similar to the CFD simulation, no vortex shedding was observed. The damping ratio was very low, though it increased when the prescribed maximum amplitude increased. This indicates that the small blade motion is the cause for this low ratio.

At the largest time step, the two-way FSI simulation showed similar pressure values and pressure contour plots were similar to 1-way FSI and transient CFD simulations. However, when the time step was reduced, instabilities were onset such that the simulation was about to crash. Moreover, the velocity profile downstream of the trailing edge matched well with each other. Though two-way FSI may be a more precise modelling approach, it may not be worthwhile in terms of how computationally costly it is, especially when time step is lowered. The structural analysis exhibited high stress regions near the trailing edge close to the hub and shroud, which was as expected. The deformation induced by the flow resembled the first bending mode shape.

The numerical simulations indicate that the design has been successful at mitigating von Kármán vortices. This is to be validated through experimental work in the future. The numerical results in this study have contributed to shed light on the fluid-structure interaction that is often observed in hydraulic turbines. More importantly, it facilitates for experimental studies on the blade cascade and as a foundation for future numerical studies on the circular blade cascade.

---

## Chapter 7

---

### **Future work**

For further work, it would be interesting to investigate a better model for the 2-way FSI. A more appropriate mesh model may ease the instabilities and allow for enough iterations that yields a converged solution. It would be interesting to test this model for the range of velocities that was planned for.

The 1-way FSI should have the mesh motion that corresponds to the critical mode shape and frequency from the harmonic response analysis. This would hopefully give a greater damping ratio. Moreover, it would be interesting to see a relationship with how increasing inlet velocity would affect the damping ratio.

Finally, higher velocities would be interesting to investigate, although this could be a too high Reynolds number, especially when it could result in cavitation. On the other hand, it would be useful information to know at what velocities cavitation is observed.



---

## References

- [1] Celik, I., Ghia, U., Roache, P., Freitas, C., Coloman, H., and Raad, P., 2008, “Procedure of Estimation and Reporting of Uncertainty Due to Discretization in CFD Applications,” *J. Fluids Eng.*, **130**.
- [2] Caridi, D., 2008, “Industrial CFD simulation of aerodynamic noise,” Ph. D., University of Naples Federico II, Napoli, Italy, doi:[dx.doi.org/10.6092/UNINA/FEDOA/3249](https://dx.doi.org/10.6092/UNINA/FEDOA/3249).
- [3] Benra, F., Dohmen, H., Pei, J., Schuster, S., and Wan, B., 2011, “A Comparison of One-Way and Two-Way Coupling Methods for Numerical Analysis of Fluid-Structure Interactions,” *Journal of Applied Mathematics*, **28**(0), pp. 1–16.
- [4] Siemonsmeier, M., Baumanns, P., van Bracht, N., Schönefeld, M., Schönbauer, A., Moser, A., Dahlhaug, O., and Heidenreich, S., 2018, “Hydropower Providing Flexibility for a Renewable Energy System: Three European Energy Scenarios. A HydroFlex report. Trondheim: HydroFlex,” .
- [5] Lewis, B., Cimbala, J., and Wouden, A. M., 2014, “Major historical developments in the design of water wheels and Francis hydroturbines,” *IOP Conference Series: Earth and Environmental Science*, **22**(1).
- [6] Sick, M., Michler, W., Weiss, T., and Keck, H., 2009, “Recent developments in the dynamic analysis of water turbines,” *SAGE Journals*, **28**(2), pp. 415–457.
- [7] Griffin, O., 1995, “A note on bluff body vortex formation,” *Journal of Fluid Mechanics*, **284**(1), pp. 217–224.

- [8] Trivedi, C., 2017, “A review on fluid structure interaction in hydraulic turbines: A focus on hydrodynamic damping,” [Engineering Failure Analysis](#), **77**, pp. 1–22.
- [9] 2019, “Dynamic Loads on Francis Turbines. An Experimental Study.” Ph. D., Norwegian University of Science and Technology, Trondheim, Norway, doi:[hdl.handle.net/11250/2596614](https://hdl.handle.net/11250/2596614).
- [10] M., S., W., M., T., W., and H, K., 2009, “Recent developments in the dynamic analysis of water turbines,” [Journal of Power and Energy](#), **223**(3), pp. 415–427.
- [11] Heskestad, G. and Olberts, D., 1960, “Influence of Trailing-Edge geometry on Hydraulic-Turbine-Blade Vibration Resulting From Vortex Excitation,” [Journal of Engineering for Power](#), **82**(2), pp. 103–109.
- [12] Coutu, A., Seeley, C., Monette, C., Nennemann, B., and Marmont, H., 2012, “Damping measurements in flowing water,” [IOP Conference Series: Earth and Environmental Science](#), **28**(4), pp. 1–9.
- [13] Liang, Q., Rodriguez, C., Egusquiza, E., Escaler, X., Farhat, M., and Avellan, F., 2007, “Numerical simulation of fluid added mass effect on a Francis turbine runner,” [Journal of Applied Mathematics](#), **36**(6), pp. 1106–1118.
- [14] Tengs, E., 2019, “Numerical simulation of the hydrodynamic damping of a vibrating hydrofoil,” Ph. D., Norwegian University of Science and Technology, Trondheim, Norway, doi:[hdl.handle.net/11250/2625210](https://hdl.handle.net/11250/2625210).
- [15] Liaghat, T., Guibault, F., Allenbach, L., and Nennemann, B., 2015, “Two-Way Fluid-Structure Coupling in Vibration and Damping Analysis of an Oscillating Hydrofoil,” [ASME 2014 International Mechanical Engineering Congress and Exposition](#), **4A**, pp. 103–109.
- [16] C., Y. A. and M., C. J., 2006, *Fluid mechanics fundamentals and applications*.
- [17] Brekke, H., 1994, “A review on oscillatory problems in Francis turbines and simulation of unsteady flow in conduit systems,” Proceedings of the 17th IAHR Symposium, Beijing, China, pp. 15–19.
- [18] Sharma, O. and Butler, T., 1987, “Predictions of Endwall Losses and Secondary Flows in Axial Flow Turbine Cascades,” [Journal of Turbomachinery](#), **109**(2), pp. 229–236.



- [19] Greitzer, E. M., Tan, C. S., and Graf, M. B., 2007, *Internal Flow: Concepts and Applications*.
- [20] Versteeg, H. K. and Malalasekera., W., 2007, *An Introduction to Computational Fluid Dynamics. 2nd edition*, Pearson Education Limited.
- [21] Pope, S., 2000, *Turbulent Flows*.
- [22] Menter, F. and Egorov, Y., 2006, “SAS turbulence modelling of technical flows,” [Direct and Large-Eddy Simulation VI](#), pp. 687–694.
- [23] Craig, R. and Kurdila, A., 2006, *Fundamentals of Structural Dynamics, 2nd Edition*.
- [24] Krommer, M., Berik, P., Vetuykov, Y., and Benjeddou, A., 2012, “Piezo-electric d15 shear-response-based torsion actuation mechanism: An exact 3D Saint-Venant type solution,” [International Journal of Smart and Nano Materials](#), **3**(2), p. 82..102.
- [25] Vu, T., Nennemann, B., Ausoni, P., Farhat, M., and Avellan, F., 2007, “Unsteady CFD Prediction of von Kármán Vortex Shedding in Hydraulic Turbine Stay Vanes,” [Infoscience](#), **284**(1), pp. 217–224.
- [26] Sagmo, K., Tengs, E., Bergan, C., and Storli, P., 2019, “PIV measurements and CFD simulations of a hydrofoil at lock-in,” [IOP Conf. Ser.: Earth Environ. Sci.](#), **240**(062006), p. 0.
- [27] *Ansys Mechanical Release 2021 R1: Mechanical User’s Guide*.
- [28] *Ansys CFD Release 2021 R1: CFX Solver Modeling Guide*.
- [29] *Ansys CFD Release 2021 R1: CFD Post’s User Guide*.
- [30] Rodriguez, C., Liang, Q., Egusquiza, E., Escaler, X., Farhat, M., and Avellan, F., 2006, “Experimental investigation of fluid added mass effect on a Francis turbine runner in still water,” [Journal of Fluids and Structures](#), **22**(5), pp. 699–712.



---

Appendices

**Appendix A – Master thesis agreement**

## Master`s Agreement / Main Thesis Agreement

<b>Faculty</b>	Faculty of Engineering
<b>Institute</b>	Department of Energy and Process Engineering
<b>Programme Code</b>	MTPROD
<b>Course Code</b>	TEP4540

<b>Personal Information</b>	
<b>Surname, First Name</b>	Jeyakaran, Roshan
<b>Date of Birth</b>	05.11.1997
<b>Email</b>	roshanje@stud.ntnu.no

<b>Supervision and Co-authors</b>	
<b>Supervisor</b>	Chirag Trivedi
<b>Co-supervisors (if applicable)</b>	
<b>Co-authors (if applicable)</b>	

<b>The Master`s thesis</b>	
<b>Starting Date</b>	
<b>Submission Deadline</b>	11.06.2022
<b>Thesis Working Title</b>	Fluid structure interaction in a blade cascade
<b>Problem Description</b>	<p>Master thesis is continuation of the project work carried out during Autumn 2021. Following research tasks are expected to complete by the candidate during Spring 2022 to qualify for the submission of the master thesis. 1. Continue on numerical modelling of blade cascade with accurate verification and validation. 2. Read literature thoroughly, specifically, fluid structure interactions in hydro turbines, blade flutter, flow separation, trailing edge vortex, stress-strain, fatigue load, resonance, mode-shape, hydrodynamic damping, natural frequency, etc. 3. Create numerical model identical to the experimental setup, which under preparation in the Waterpower Laboratory. 4. Investigate flow field with in the blade cascade with one-way and two-way fluid structure interactions, including modal and harmonic analysis. If time available, join laboratory experimentation in the laboratory. 5. Combine all research results and, if time available, aim to write a research article for the possible submission in a selected academic journal. Deliver the master thesis before the deadline in Spring 2022.</p>

Risk Assessment and Data Management	
<b>Will you conduct a Risk Assessment?</b>	No
<b>If “Yes”, Is the Risk Assessment Conducted?</b>	No
<b>Will you Apply for Data Management? (REK*, NSD**)</b>	No
<b>Will You Write a Confidentiality Agreement?</b>	No
<b>If “Yes”, Is the Confidentiality Agreement Conducted?</b>	No

\* REK -- <https://rekportalen.no/>

\*\* Norwegian Centre for Research Data (<https://nsd.no/nsd/english/index.html> )

Topics to be included in the Master`s Degree (if applicable)



---

## Appendices

---

### Appendix B – MATLAB code for FFT

```
close all
clear
clc

%cd 'Monitor Point Output'/'
MP1 = readtable('vel_ifsi.csv'); %read exported file from solver CFX
iter = MP1{:,1}; %iteration number
phi_Fluct = MP1{:,2}; %2nd column, where Pfluct data is
L = length(phi_Fluct); %length of vector
dt = 5.3449E-06;%1-way FSI
Fs = (1/dt); %sample frequency = 1/dt
f = Fs*(0:(L/2))/L; %frequency interval
Y=fft(detrend(phi_Fluct)); %assign fft of pfluct to Y

P2 = abs(Y/L); %convert to one-sided spectrum
P1 = P2(1:L/2+1); %
P1(2:end-1) = 2*P1(2:end-1);

%%
MP2 = readtable('vel_cfd.csv');
iter2 = MP2{:,1};
phi = MP2{:,2};
len = length(phi);
time = 1E-5;
freq = 1/time;
fi = freq*(0:(len/2))/len;
Y2 = fft(detrend(phi));
```

```

q2 = abs(Y2/len);
q1 = q2(1:len/2+1);
q1(2:end-1) = 2*q1(2:end-1);

%%
figure(1)
plot(f,P1,'k')
title('FFT of velocity from 1-way FSI','interpreter','latex')
xlabel('Frequency [Hz]','interpreter','latex')
ylabel('Amplitude [ms-1]', 'interpreter','latex')
set(gca,'XLim', [0 50000]);

figure(2)
plot(fi,q1,'k')
title('FFT of velocity from transient CFD at 13ms-1','interpreter','latex')
xlabel('Frequency [Hz]','interpreter','latex')
ylabel('Amplitude [ms-1]', 'interpreter','latex')
set(gca,'XLim', [0 10000]);
%{
function [Amp f] = FFTpwelch(x,Fs, varargin)

nfft = length(x);
k = length(varargin);

if isempty(varargin)
    window = hanninf(nfft);
    noverlap = 0.5*nfft;
elseif k ==1
    in = varargin{1};
    estimateF = 1/in(1)*Fs;
    if length(in) == 2
        segmentsize=round(estimateF*in(2));
    else
        segmentsize=round(estimateF*10);
    end
    window = hanning(segmentsize);
    noverlap = 0.5*segmentsize;
elseif k==2
    window = varargin {2};
    noverlap = 0.5* length ( window );

```



```

else k ==3;

    window = varargin {2};
    noverlap = varargin {3}* length ( window );
end
windowp = window;
noverlap2 = noverlap;
probability = 0.95;
[pxx ,f, pxxc ] = pwelch (x,window , noverlap ,nfft ,Fs ,' ConfidenceLevel ',pr
S1=sum ( window );
S2=sum ( window .^2) ;
ENBW =Fs *( S2 /( S1 ^2) ); % Power spectrum
Amp = sqrt (pxx )* sqrt (2) ;

end
%}

```



---

## Appendices

---

### Appendix C - Ansys codes

#### C.1 Ansys code for material properties and mesh type

```
!material properties and mesh
```

```
et,MATID,SOLID227,1001
```

```
!226 for hex, 227 for tetra
```

```
mp,perx,MATID,926 d
```

```
mp,pery,MATID,926
```

```
mp,perz,MATID,794
```

```
tb,piez,MATID
```

```
tbddata, 5, 11.9 ! e15
```

```
tbddata, 10, 11.9 ! e24
```

```
tbddata, 13, -7.5 ! e31
```

```
tbddata, 14, -7.5 ! e32
```

```
tbddata, 15, 13.7 ! e33
```

#### C.2 Voltage load application

```
!d - dielectric
```

```
!Hydrofoil 1
```

```
d, HF1_POS1, VOLT, 1 !positive side of MPC
```

```
d, HF1_NEG1,VOLT,0 !negative side (grounded) of MPC
```

```

d, HF1_POS2, VOLT, 1
d, HF1_NEG2,VOLT,0

!d - dielectric
!Hydrofoil 2
d, HF2_POS1, VOLT, 1      !positive side of MPC
d, HF2_NEG1,VOLT,0       !negative side (grounded) of MPC
d, HF2_POS2, VOLT, 1
d, HF2_NEG2,VOLT,0

!d - dielectric
!Hydrofoil 3
d, HF3_POS1, VOLT, 1      !positive side of MPC
d, HF3_NEG1,VOLT,0       !negative side (grounded) of MPC
d, HF3_POS2, VOLT, 1
d, HF3_NEG2,VOLT,0

!d - dielectric
!Hydrofoil 4
d, HF4_POS1, VOLT, 1      !positive side of MPC
d, HF4_NEG1,VOLT,0       !negative side (grounded) of MPC
d, HF4_POS2, VOLT, 1
d, HF4_NEG2,VOLT,0

!d - dielectric
!Hydrofoil 5
d, HF5_POS1, VOLT, 1      !positive side of MPC
d, HF5_NEG1,VOLT,0       !negative side (grounded) of MPC
d, HF5_POS2, VOLT, 1
d, HF5_NEG2,VOLT,0

!d - dielectric
!Hydrofoil 6
d, HF6_POS1, VOLT, 1      !positive side of MPC
d, HF6_NEG1,VOLT,0       !negative side (grounded) of MPC
d, HF6_POS2, VOLT, 1
d, HF6_NEG2,VOLT,0

!d - dielectric
!Hydrofoil 7
d, HF7_POS1, VOLT, 1      !positive side of MPC

```

```
d, HF7_NEG1,VOLT,0      !negative side (grounded) of MPC
d, HF7_POS2, VOLT, 1
d, HF7_NEG2,VOLT,0

!d - dielectric
!Hydrofoil 1
d, HF8_POS1, VOLT, 1    !positive side of MPC
d, HF8_NEG1,VOLT,0     !negative side (grounded) of MPC
d, HF8_POS2, VOLT, 1
d, HF8_NEG2,VOLT,0
```

